PHYSICAL REVIEW C, VOLUME 64, 014607

Mass distributions in nucleon-induced fission at intermediate energies

M. C. Duijvestijn* and A. J. Koning
Nuclear Research and Consultancy Group, Westerduinweg 3, NL-1755 ZG Petten, The Netherlands

F.-J. Hambsch†
EC-JRC Institute for Reference Materials and Measurements, Retieseweg, B-2440 Geel, Belgium

(Received 16 October 2000; published 11 June 2001)

Temperature-dependent fission barriers and fission-fragment mass distributions are calculated in the framework of the multimodal random neck-rupture model (MM-RNRM). It is shown how the distinction between the different fission modes disappears at higher excitation energies, due to the melting of shell effects. The fission-fragment mass yield calculations are coupled to the nuclear reaction code ALICE-91, which takes into account the competition between the other reaction channels and fission. With the combination of the temperature-dependent MM-RNRM and ALICE-91 nucleon-induced fission is investigated at energies between 10 and 200 MeV for nuclei varying from Au to Am.

DOI: 10.1103/PhysRevC.64.014607 PACS number(s): 24.75.+i, 25.85.Ec, 25.85.Ge

I. INTRODUCTION

Almost since the time of its discovery, applied and academical interests in the nuclear fission process go hand in hand. Historically, most of the effort has been put into the development of the fission knowledge at low energies. To a lesser extent, also fission reactions induced by neutrons and charged particles at intermediate incident energies, i.e., between 10 and 200 MeV, have been investigated. Research in this field of intermediate-energy fission is nowadays stimulated by the world-wide attention drawn towards accelerator-driven systems (ADS) for the transmutation of nuclear waste and other purposes, such as the production of energy and radioisotopes. Whereas in most conventional nuclear applications particle energies are limited to several MeV, in these ADS concepts energies up to the GeV region are playing an important role. Feasibility studies of ADS designs require knowledge of all the underlying nuclear reactions that constitute a significant part of the reaction cross section. This comprises both proton and neutron-induced reactions ranging in energy from thermal up to a GeV. One of the processes that occurs both in the target and the reactor core is fission. Figure 1 shows the reaction cross sections and the fission cross sections at incident neutron energies up to 300 MeV for ^{209}Bi and ^{238}U. This reveals that about 5% of the reaction flux goes into the fission channel for bismuth and more than 50% for uranium. Fission of actinides as well as subactinides is not yet understood sufficiently for incoming energies above a few MeV. Compared to spallation and evaporation cross sections the subactinide fission cross section is relatively small. This contribution should, however, be taken into account for a proper computational analysis of the target and its direct environment, where undesired radioactive isotopes may be produced. It depends on the design of the ADS [1], whether the neutrons entering the reactor core do have a significant intermediate-energy tail or not. At energies above 200 MeV, the neutron flux inside the core surely diminishes rapidly. As for many aspects of the ADS design, the role of intermediate-energy actinide fission is, therefore, not yet clear. Nevertheless, an adequate answer for intermediate-energy fission must be provided, before sensitivity studies can probe its true significance.

From the more fundamental point of view, fission remains an intriguing object of study as well. In fission at intermediate energies two factors emerge that complicate the description in comparison with low-energy fission: multichance fission and the varying fission characteristics with excitation energy. Fission being a relatively slow process that involves a collective deformation of the entire nucleus, is likely to compete with particle evaporation. In addition, at high incident energies it will most probably be preceded by fast emission of particles in a directlike mechanism. This immediately illustrates the complexity of the process: a large number of intermediate nuclides, each with its own fission characteristics, are formed in the neighborhood of the original target nucleus. They all contribute to the experimental fission observables and make it incredibly difficult or even impossible to disentangle from this superposition the information on the fission properties of the separate nucleus. Figure 2 serves to illustrate the difference between the first-chance process, characteristic for low-energy fission, and the multichance process playing an important role in intermediate-energy fission. If the energy of the incoming nucleon is low, the slightly excited compound nucleus starts to deform and may ultimately fission before it has emitted any particles. This process produces two fragments F_1 and F_2 with nucleon numbers that sum up to the original number of nucleons present in the compound nucleus. The fragments are excited and lose, subsequently, their energy by the evaporation of nucleons and gammas. In the end, two fission products P_1 and P_2 remain. On the other hand, if the excitation energy in the compound system is high enough, the nucleus will emit $n+1$ nucleons during the fast stage of the reaction followed by the emission of m particles in the evaporation stage. The fissioning nucleus is characterized by a nucleon number $A-n-m$. Fission fragments F_1' and F_2' are formed, which

---

*Electronic address: duijvestijn@nrg-nl.com

†Electronic address: hambsch@irmm.jrc.be

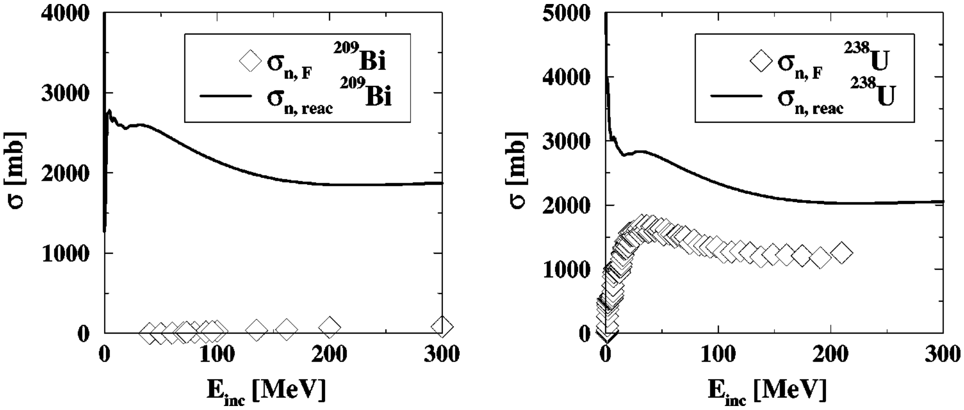

FIG. 1. Reaction cross sections as a function of incident neutron energy compared to the fission cross sections for ^{209}Bi and ^{238}U. The reaction cross sections are obtained from an optical model by Ref. [2] and the experimental data for the fission cross sections are taken from Refs. [3–5].

evaporate an additional number of particles, and hence create the fission products P'_1 and P'_2.

In the past, several attempts have been made to describe and understand the varying fission characteristics of nuclides with excitation energy (e.g., Refs. [6–10]). An overview can be found in Ref. [11]. Moreover, Brosa *et al.* [12] have developed a model which is elucidated in great detail in the remainder of this paper. In summary, the competition between symmetric and asymmetric fission is thought to be connected to shell effects in the deformed nucleus. The presence of these shell structures leads to the existence of symmetric and asymmetric fission modes or channels, which a nucleus can choose to follow on its way to fission. It is the contribution of each fission mode that changes with excitation energy. In addition, shell effects fade with higher excitation energy resulting in a nucleus which possesses merely a symmetric fission mode. As a result of these properties, actinides near the valley of stability prefer asymmetric fission at low energies, but are subject to an increasing contribution of symmetric fission at increasing energies. Further away in the neutron-deficient region, the actinide nuclides tend to fission symmetrically even at lower excitation energies [7,13]. In the subactinide region the symmetric fission mode is already the strongest mode at small energies and remains the dominant channel at higher excitation energies. Despite all the progress in the understanding of the fission process, a lot of questions remain. After 60 years of research, still no theory or model is able to describe the mass dependent and excitation energy dependent transition between asymmetric and symmetric fission in a satisfactory way, and to predict all the fission observables in one consistent approach for all possible fissioning systems in going from low to high excitation energies.

Some models (e.g., Refs. [14,15]) (partly) rely on systematics in order to predict fission-product yields at intermediate energies. The lack of experimental data hampers the development of systematics for quantities like the symmetric and asymmetric fission contributions or the fission-fragment mass and charge distributions in a wide range of nuclides and energies. In addition, the measured results for intermediate-energy fission arise as a superposition of many contributing fissioning systems characterized by their own excitation energy distributions. Since the disentanglement of all these separate contributions is impossible, the comparison between the calculated and the experimental results cannot take place at this level. It has to be carried out for the summed observables instead. In this manner, trends in the separate contributions are taken into account in an effective way in the systematics in order to arrive at a description of the experimental results. This may lead to wrong results when systematics is extrapolated into a region without experimental data. Therefore in this work much effort is in-

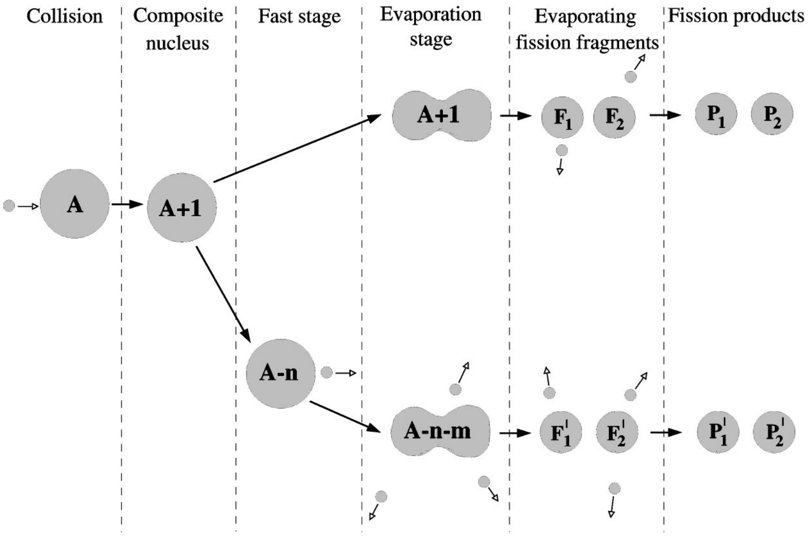

FIG. 2. Schematical drawing illustrating the difference between first-chance fission (upper branch) and multichance fission (lower branch). A denotes the nucleon number of the bombarded nucleus, n+1 and m the number of emitted nucleons, F a fission fragment, and P a fission product.

vested in the development of a more fundamental approach. The hope stands that the physics incorporated in such an approach ensures better predictive properties independent of the presence of experimental data.

The objective of our work is to compute fission-fragment and fission-product mass yields from intermediate-energy nucleon-induced reactions. In the approach presented here two stages can be distinguished. In the first stage the fission cross section is determined for the various fissioning isotopes as a function of their excitation energy in competition with other processes like pre-equilibrium decay and particle evaporation (Sec. III). ALICE-91 is a nuclear reaction code that takes care of this first stage. The second stage consists of constructing the total fission-fragment mass distributions from the different contributions of all the equilibrated fissioning systems. Hence a model is needed that gives a prediction for the fission-fragment mass yields in a large range of mass, charge, and excitation energy of the fissioning nucleus. For this purpose, the multimodal random neck-rupture model by Brosa [12] is extended with temperature-dependent shell and pairing corrections and a temperature-dependent liquid drop model (LDM) for the calculation of a temperature-dependent potential energy surface. Subsequently, the resulting temperature-dependent barriers are employed to determine the relative contributions of the different fission modes. This is described in great detail in Sec. II. Section IV contains the coupling between ALICE-91 and the revised Brosa model as well as the results obtained in this manner. Finally, a summary and an outlook may be found in Sec. V.

II. TEMPERATURE-DEPENDENT BROSA MODEL

The theoretical analysis of experimental fission-fragment and fission-product mass distributions presented here is largely built around the multimodal random neck-rupture model (MM-RNRM), or Brosa model as it is commonly called. This model has been developed by Brosa *et al.* [12,16] in the 1980s to explain fission at very low energies. It consists of two complementary descriptions: the multichannel evolution to scission and the random neck-rupture model (RNRM). The evolution towards scission can take place along several paths of disintegration of the nucleus, the so-called fission channels. At the end of such a channel the nucleons find themselves in an elongated configuration of two preformed fragments connected by a neck: the prescission shape. If the nucleus stretches beyond this prescission shape the neck will snap according to the RNRM. This results in two nascent fission fragments.

In many fission theories, each nucleus possesses one single or double-humped barrier on its way to scission. In the Brosa model, however, the nucleus may, starting from its ground state, choose between various paths of minimal deformation energy on its journey through deformation space. Each path belongs to a certain fission mode. It leads along its own hills in the potential energy landscape and arrives at its own set of deformation parameters fixing the prescission shape corresponding to that particular fission mode. This idea of parallel fission barriers and channels builds on the work by Turkevich and Niday [17], who interpreted the mass yield distribution of thorium as a superposition of two fission channels, and of Pashkevich [18], who discovered two fission modes in lead in his calculations. For most actinide nuclei three dominant fission modes exist: the symmetric superlong (SL) and the asymmetric standard I (ST I) and standard II (ST II) modes. These asymmetric modes are generally thought to be linked with the neutron shells in the fragments of $N=82$ (spherical) for ST I and $N=88$ (deformed) for ST II.

As indicated above, each channel corresponds to its own class of prescission shapes. These shapes convey indirectly the properties of the fission fragments. For example, an asymmetric shape gives rise to an asymmetric mass division, and a very compact shape results in a high kinetic energy of the fragments. The random neck-rupture model quantizes this information, and links the prescission shapes with the properties of the fission fragments like the total kinetic energy (TKE), the mass distribution, the most probable charge and the postscission neutron multiplicities. This is treated in Sec. II G. An elaborate description of the complete Brosa model can be found in Ref. [12].

For the calculation of these fission channels, it is necessary to minimize the deformation energy of the nucleus at the potential energy surface (PES). In the original Brosa model, this is done for zero temperature. Therefore, strictly speaking, only fission at zero excitation energy, i.e., spontaneous fission, can be treated within this approach. Since the PES does not change much at low energies, the use of the original Brosa model in the analysis of low-energy neutron-induced fission is still justified. However, for the description of intermediate-energy fission an extension of the model is clearly indispensable. In this work the PES is computed as a function of the temperature of the nucleus (see Sec. II A). Minimization at the PES provides the fission channels, and hence the fission barriers as a function of temperature. The PES changes drastically with temperature: asymmetric fission modes melt together and disappear for high excitation energies, and double-humped barriers transform to single humped. The use of temperature-dependent fission barriers is elucidated in Sec. II E and the influence of temperature at the barriers and the prescission shapes is discussed in II D and II F. Another addition to the Brosa model consists of the calculation of the weight for different contributing fission modes based on the transmission through the parallel barriers. At the end of this section, the mass distributions of the fission fragments and products can be determined for a given excitation energy of the fissioning nucleus.

A. Potential energy surface

The deformation energy is obtained with the macroscopic-microscopic method due to Strutinsky [19]:

$$E=E_{LDM}+\delta E_{shell}. \tag{1}$$

The basic ingredients are the liquid drop energy and the shell correction term. The liquid drop part contains the macroscopic smooth behavior of the energy, whereas the microscopic shell effects are added as a correction. In principle, the potential energy of a nucleus can also be obtained directly from a microscopic approach. Strutinsky recognized that a greater accuracy is achieved by using a liquid drop model (LDM) for the description of the smooth background behavior of the energy. Such a model is tuned to reproduce experimental masses. It is therefore impossible to outperform the liquid drop outcome for global properties with a microscopic model like the one that will be sketched in Sec. II A 2. The macroscopical nature of the LDM necessitates the addition of shell corrections for a more detailed description of the nucleus, which takes the effect of the filling of single particle levels into account.

Equation (1) can be generalized as a function of temperature T and deformation def:

$$F(T,\text{def}) = F_{LDM}(T,\text{def}) + \delta F_{shell}(T,\text{def}). \tag{2}$$

The energy E of expression (1) is replaced by the free energy F, which represents the potential energy for isothermal processes. The free energy is linked to the internal energy through the entropy S:

$$F(T,\text{def}) = E(T,\text{def}) - TS(T,\text{def}). \tag{3}$$

The use of the free energy implies that the deformation of the nucleus is assumed to be an isothermal process.

1. Generalized Lawrence shapes

In following a nucleus on its way to scission, a parametrization of its shape is required, which is able to describe all possible deformations between the (spherical) ground state and the elongated (asymmetric) prescission shape that consists of the two preformed fragments linked by a neck. The Brosa model employs the generalized Lawrence shapes [20] to parametrize the deforming nucleus:

$$\rho^2(\zeta) = (l^2 - \zeta^2) \sum_{n=0}^{N} a_n (\zeta - z)^n. \tag{4}$$

The radius of the nucleus is given by ρ as a function of a parameter ζ. Five shape parameters, with a geometrical meaning as depicted in Fig. 3, fix the coefficients a_n ($n = 0 \ldots 4$):

$$l, r, z, c, s. \tag{5}$$

The semilength l is a measure of the elongation of the nucleus. The neck radius is denoted by r. In the case of a spherical ground state, l and r coincide with the compound nucleus radius r_{CN}. The parameter z gives the position of the thinnest point at the neck or the thickest point of the shape if the neck is not present. The curvature of the neck is given by $c = r_{CN}^2 / r_{curv}$ with r_{curv} the curvature radius. The fifth parameter s denotes the position of the centroid. The plane $\zeta = 0$ in Fig. 3 is defined by cutting the nucleus in two pieces with equal length.

These five degrees of freedom are connected to the coefficients a_n ($n = 0 \ldots 4$) through some simple boundary conditions: the neck radius should equal r at $\zeta = z$, the first derivative should be zero at $\zeta = z$, the second derivative is related to the curvature at $\zeta = z$, volume conservation, and through the definition of center of mass.

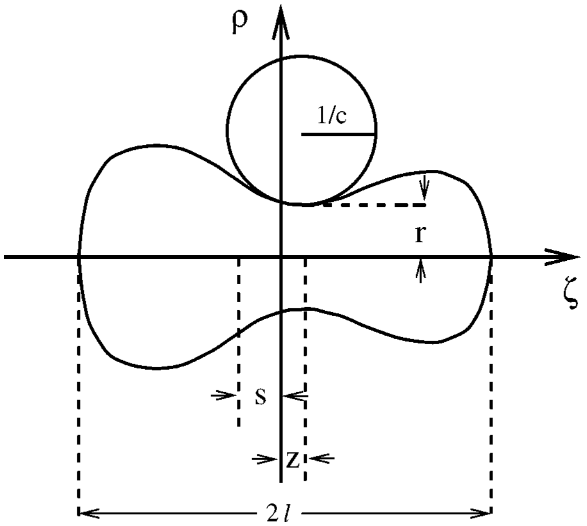

FIG. 3. The geometrical meaning of the five degrees of freedom l, r, z, s, and c.

Other parameters that are frequently used and which may be derived from the parametrization above are A_h and d. The average mass of the heavy fragment is given by

$$A_h = \frac{3A_{CN}}{4r_{CN}^3} \int_{-l}^{z} \rho^2(\zeta)\, d\zeta. \tag{6}$$

A_{CN} is the mass number of the compound nucleus. The parameter d measures the distance between the centers of mass of the average left and right fragments. It is defined analogously to Eq. (6).

Another possibility would have been to use a parametrization that also generates configurations like touching spheroids (e.g., the parametrization used in Ref. [21]). Since, however, each channel search stops at a prescission shape characterized by two preformed fragments still linked by a neck, it was not deemed necessary to employ such a parametrization in this stage of the calculation. In a later stage, the RNRM deals with the touching spheroids that emerge at the scission point. This parametrization can be found in Sec. II G 2.

2. Temperature-dependent shell and pairing effects

The investigation of temperature effects on the shell correction term in Eq. (2) can be subdivided into three steps. Initially, the single-particle energies of the system have to be extracted from a Hamiltonian without pairing. Subsequently, the BCS pairing theory provides expressions for quantities like the internal energy, entropy and free energy of the system, which are based on this unperturbed discrete single-particle energy spectrum. This step introduces the pairing effect, and the dependence on temperature. The quantities obtained represent the properties of a real quantal system; they alter abruptly with nucleon number and contain all shell effects. During the third step, the shell-dependent behavior of each quantity is isolated. This is done by subtraction of a counterpart describing the smooth background. This smooth counterpart remains after the evaluation of the same BCS expressions with a *smooth* level density, instead of the *discrete* level density. It varies continuously with nucleon number and has lost all information on the shell structure. The discrete single-particle energy spectrum is smeared to construct this smooth level density. The procedure to disentangle the shell effects and the continuous behavior has been developed by Strutinsky [19]. All steps are carried out for neutrons and protons separately. The outcomes are added to give a total shell-plus-pairing correction as a function of temperature.

In the first step the single-particle energies for a system without pairing are obtained by solving the Schrödinger equation for the following Hamiltonians:

$$H_n=\frac{\mathbf{p}^2}{2M_n}+V_n(\mathbf{r})-\frac{\lambda}{2(M_nc)^2}\mathbf{s}\cdot[\nabla V_n(\mathbf{r})\times\mathbf{p}], \tag{7}$$

$$H_z=\frac{\mathbf{p}^2}{2M_z}+V_z(\mathbf{r})-\frac{\lambda}{2(M_zc)^2}\mathbf{s}\cdot[\nabla V_z(\mathbf{r})\times\mathbf{p}]+V_{Coul}(\mathbf{r}). \tag{8}$$

Here the labels *n* and *z* denote neutrons and protons, respectively. **p** and **s** corresponds to the vector operators for momentum and spin, *M* to the nucleon mass, and $V(\mathbf{r})$ to the single-particle potential which is chosen to be of Woods-Saxon type:

$$V_{n,z}(\rho,\zeta)=\frac{V_{0,n,z}}{1+\exp[(L(\rho,\zeta)-R)/a]}. \tag{9}$$

The spin-orbit strength λ, the radius *R*, and the diffuseness *a* are identical for neutrons and protons:

$$\lambda=23.8\frac{1+2(N_{CN}-Z_{CN})}{A_{CN}}, \tag{10}$$

$$R=1.24A_{CN}^{1/3}\ \text{fm}, \tag{11}$$

$$a=0.63\ \text{fm}, \tag{12}$$

with N_{CN}, Z_{CN}, and A_{CN} the neutron, proton, and nucleon numbers of the fissioning nucleus. The depths of the potentials are charge dependent:

$$V_{0,z,n}=53.3\left[1\pm0.63\frac{(N_{CN}-Z_{CN})}{A_{CN}}\right], \tag{13}$$

where the plus sign is for protons and the minus sign for neutrons. The parameters for this average Woods-Saxon field for neutrons and protons are taken from Ref. [22]. The Coulomb potential experienced by a proton is given by

$$V_{Coul}(\mathbf{r})=\frac{3Z_{CN}e^2}{4\pi R^3}\int_{nucleus}\frac{d^3\mathbf{r}'}{|\mathbf{r}-\mathbf{r}'|}. \tag{14}$$

The function $L(\rho,\zeta)$ appears as the numerical solution of

$$\rho_{shape}(\zeta R/L;l,r,z,c,s)=\rho R/L. \tag{15}$$

In this manner, the potential in Eq. (9) is adjusted to the actual shape of the nucleus as given in Sec. II A 1. A detailed description of how the eigenvalues of Eqs. (7) and (8) are obtained from the Schrödinger equation can be found in Ref. [12].

As already pointed out in the beginning of this section, the next step introduces both pairing and temperature. The implementation of the temperature-dependent BCS model is done in a standard way [23–26]. The derivation of the expressions for the temperature-dependent internal energy, the free energy and entropy, starts from the well-known BCS Hamiltonian

$$H^{BCS}=\sum_k \epsilon_k a_k^\dagger a_k-G\sum_{k,k'>0}a_{-k}^\dagger a_k^\dagger a_{k'}a_{-k'}, \tag{16}$$

where ϵ_k are the unperturbed single-particle energies levels labeled by the quantum number *k* and obtained from the Hamiltonian (7) and (8). *G* gives the strength of the pairing interaction and $a_k^\dagger, a_k$ are the single-particle creation and annihilation operators. The pairing force is assumed to be constant and acts only in a range of $\sqrt{3N}$ single-particle levels below and above the Fermi energy (with *N* the proton or neutron number). The chosen value for the pairing strength is

$$G=34/A_{CN}\ \text{MeV}. \tag{17}$$

In order to ensure, on the average, a constant number of particles, the following new Hamiltonian is considered:

$$H\rightarrow H-\lambda_F N, \tag{18}$$

with *N* the number of particles and λ_F a Lagrangian multiplier. Subsequently, thermal excitation can be introduced into the description with the aid of the grand canonical formalism. To a good approximation the grand potential Ω can be expressed as

$$\Omega=-T\ln\mathcal{Z}=\sum_{k>0}(\epsilon_k-\lambda_F-\epsilon_{qp})-2T\sum_{k>0}\ln\left[1+\exp\left(-\frac{\epsilon_{qp}}{T}\right)\right]+\frac{\Delta^2}{G}. \tag{19}$$

In this formula, $\mathcal{Z}$ is the grand partition function, and *T* the temperature measured in energy units. The quasiparticle energy is given by

$$\epsilon_{qp}=\sqrt{(\epsilon_k-\lambda_F)^2+\Delta^2}. \tag{20}$$

The gap parameter $\Delta(T)$ and the Fermi energy $\lambda_F(T)$ are fixed by the coupled gap and particle number conservation equations

$$\frac{2}{G}=\sum_{k>0}\frac{1}{\epsilon_{qp}}\tanh\left(\frac{\epsilon_{qp}}{2T}\right), \tag{21}$$

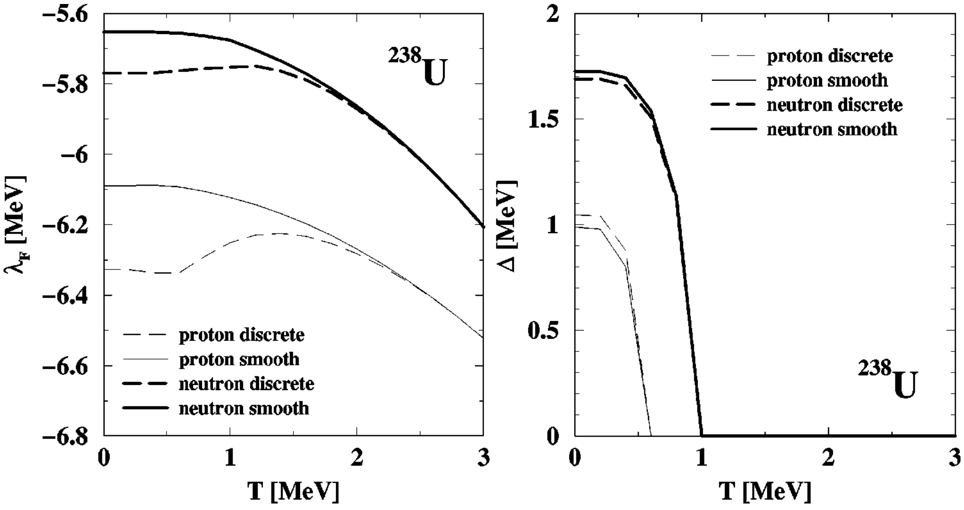

FIG. 4. The left panel shows the discrete and smooth Fermi energy for protons and neutrons as a function of temperature. The right panel contains the discrete and smooth pairing gap for protons and neutrons as a function of temperature. Both plots contain data for ^{238}U in its ground state.

$$N^{BCS}(\mathrm{def},T)=-\frac{\partial\Omega}{\partial\lambda_F}=\sum_{k>0}\left[1-\frac{\epsilon_k-\lambda_F}{\epsilon_{qp}}\tanh\left(\frac{\epsilon_{qp}}{2T}\right)\right]. \tag{22}$$

Although it is not explicitly indicated, all the quantities on the right (except the temperature) depend on deformation. Equations (21) and (22) can be solved numerically for different values of *T*. The obtained quantities are called *discrete* since they result from solving the equations with the discrete single-particle energy spectrum. In Fig. 4 the behavior of the discrete gap and the discrete Fermi energy as a function of temperature is plotted for ^{238}U at the ground-state deformation. Above a certain critical temperature T_c the pairing gap becomes zero (right panel in Fig. 4). At higher temperatures pairing no longer plays a role. This value for T_c is smaller for protons than for neutrons, just like the pairing gap itself. From the plot of the Fermi energy (left panel in Fig. 4) it can be concluded that for this beta-stable nucleus, the proton Fermi level is more deeply bound than the neutron Fermi level. At higher temperatures more nucleons occupy levels above the Fermi energy with higher level densities, thereby lowering the value of $\lambda_F(T)$. In the original Brosa model, Eqs. (21) and (22) are solved for the case $T=0$, which simplifies the equations considerably. For the temperature-dependent version of the Brosa model, it is necessary to solve the full equations. This forms one of the main additions to the original Brosa model in this work. Knowing the pairing gap and the Fermi energy, all other quantities of interest are now within reach:

$$E^{BCS}(\mathrm{def},T)=\sum_{k>0}\epsilon_k\left[1-\frac{\epsilon_k-\lambda_F}{\epsilon_{qp}}\tanh\left(\frac{\epsilon_{qp}}{2T}\right)\right]-\frac{\Delta^2}{G}, \tag{23}$$

$$S^{BCS}(\mathrm{def},T)=2\sum_{k>0}\left\{\ln\left[1+\exp\left(-\frac{\epsilon_{qp}}{T}\right)\right]+\frac{\epsilon_k/T}{1+\exp(\epsilon_k)}\right\}, \tag{24}$$

$$F^{BCS}(\mathrm{def},T)=E^{BCS}(\mathrm{def},T)-TS^{BCS}(\mathrm{def},T). \tag{25}$$

E^{BCS} is the BCS internal energy, S^{BCS} the BCS entropy, and F^{BCS} the BCS free energy.

All the quantities derived above comprise the full shell-dependent behavior. In order to distill the shell-plus-pairing effect, the smooth counterpart of each quantity has to be subtracted. For instance, the internal energy correction term equals

$$\delta E(\mathrm{def},T)=E^{BCS}(\mathrm{def},T)-\tilde{E}^{BCS}(\mathrm{def},T). \tag{26}$$

The second term is the smooth internal energy:

$$\tilde{E}^{BCS}(\mathrm{def},T)=\int_{-\infty}^{\infty}d\epsilon\tilde{g}(\epsilon)\epsilon\left[1-\frac{\epsilon-\tilde{\lambda}_F}{\tilde{\epsilon}_{qp}}\tanh\left(\frac{\tilde{\epsilon}_{qp}}{2T}\right)\right]-\frac{\tilde{\Delta}^2}{G}, \tag{27}$$

which results from averaging Eq. (23) over an energy interval γ by using the smoothed level density $\tilde{g}(\epsilon)$. The sharp level density simply equals a sum of delta functions,

$$g(\epsilon)=\sum_k n_k\delta(\epsilon-\epsilon_k), \tag{28}$$

in which n_k denote the multiplicities of the single-particle energies ϵ_k. The smeared level density looks as follows:

$$\tilde{g}(\epsilon)=\frac{1}{\sqrt{\pi}\gamma}\sum_k n_kP_6\left(\frac{|\epsilon-\epsilon_k|}{\gamma}\right)\exp\left[-\left(\frac{\epsilon-\epsilon_k}{\gamma}\right)^2\right]. \tag{29}$$

The derivation of the polynomial

$$P_6(x)=-\frac{1}{6}x^6+\frac{7}{4}x^4-\frac{35}{8}x^2+\frac{35}{16}, \tag{30}$$

suitable for the smearing purpose, can be found in Ref. [27]. The smearing parameter γ is fixed at 8.0 MeV. The chemical potential and pairing gap in Eq. (27) are obtained from the smoothed versions of Eqs. (21) and (22):

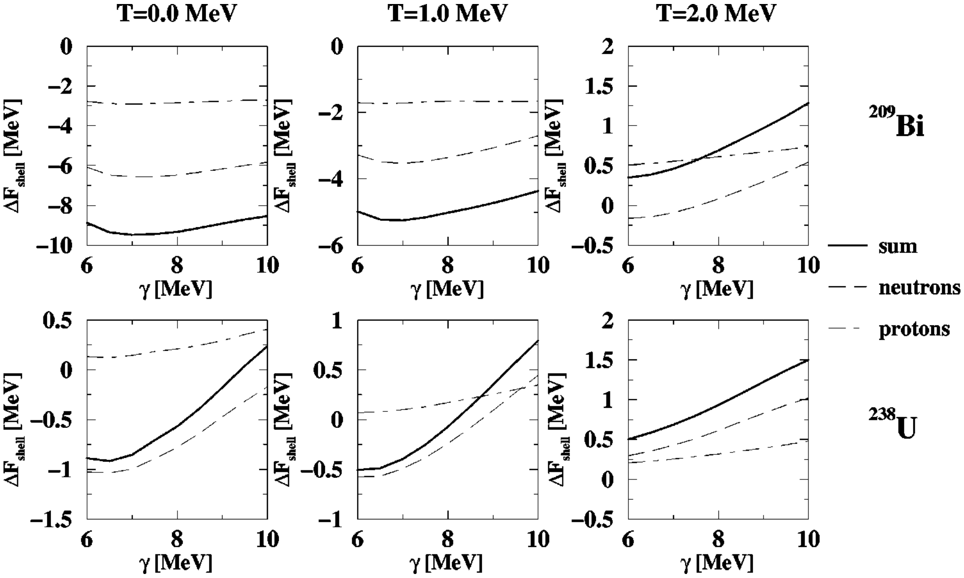

FIG. 5. The shell-plus-pairing correction to the free energy as a function of the value for the smearing parameter γ for ^{209}Bi and ^{238}U in their ground states, and for three temperatures.

$$\frac{2}{G}=\int_{-\infty}^{\infty} d\epsilon\,\tilde{g}(\epsilon)\,\frac{1}{\tilde{\epsilon}_{qp}}\tanh\left(\frac{\tilde{\epsilon}_{qp}}{2T}\right) \qquad (31)$$

$$N^{BCS}(\text{def},T)=\int_{-\infty}^{\infty} d\epsilon\,\tilde{g}(\epsilon)\left[1-\frac{\epsilon-\tilde{\lambda}_F}{\tilde{\epsilon}_{qp}}\tanh\left(\frac{\tilde{\epsilon}_{qp}}{2T}\right)\right]. \qquad (32)$$

The smoothed pairing gap and Fermi energy plotted in Fig. 4 exhibit a similar behavior as the discrete quantities, and they give rise to a smoothed quasiparticle energy $\tilde{\epsilon}_{qp}=\sqrt{(\epsilon_k-\tilde{\lambda}_F)^2+\tilde{\Delta}^2}$. Analogously, the smoothed entropy $\tilde{S}^{BCS}(\text{def},T)$ and free energy $\tilde{F}^{BCS}(\text{def},T)$ can be derived. As a consequence, the shell correction for the entropy and free energy can be written down:

$$\delta S(\text{def},T)=S^{BCS}(\text{def},T)-\tilde{S}^{BCS}(\text{def},T), \qquad (33)$$

$$\delta F(\text{def},T)=\delta E(\text{def},T)-T\,\delta S(\text{def},T). \qquad (34)$$

In Fig. 5 the shell-plus-pairing correction to the free energy is illustrated as a function of the value for the smearing parameter γ. Results for ^{238}U and ^{209}Bi in their ground states and for three different temperatures are shown. According to Brosa *et al.* [12], a plateau exists between 6 and 10 MeV for γ. Results for bismuth confirm this behavior. Nevertheless, for uranium the neutron shell-plus-pairing correction exhibits a variation of approximately 1 MeV. The conclusion has to be that the Strutinsky method, as it is implemented here, has an accuracy which is not better than about 1 MeV.

In Fig. 6 the shell-plus-pairing correction to the free energy is shown as a function of temperature for protons and neutrons separately for the ground-state deformation of ^{209}Bi and ^{238}U as well as for the outer symmetric saddle-point deformation of ^{238}U. The ground-state shell corrections are strong and negative for ^{209}Bi due to the almost double shell closure. In ^{238}U the ground-state shell effects are practically zero, whereas the shell effects are largely positive at the top of the outer barrier. Above $T=1$ MeV the shell correction drops, until it vanishes at temperatures higher than $T=2$ MeV. In Fig. 4 around these temperatures the same changes are visible in the Fermi energy. The difference between the smooth and the discrete Fermi energy remains more or less constant up to 1 MeV, and disappears at higher energies.

3. Temperature-dependent liquid drop model

The LDM employed in the original Brosa model is taken from Myers and Swiatecki [28]. The energy is given by the following formula:

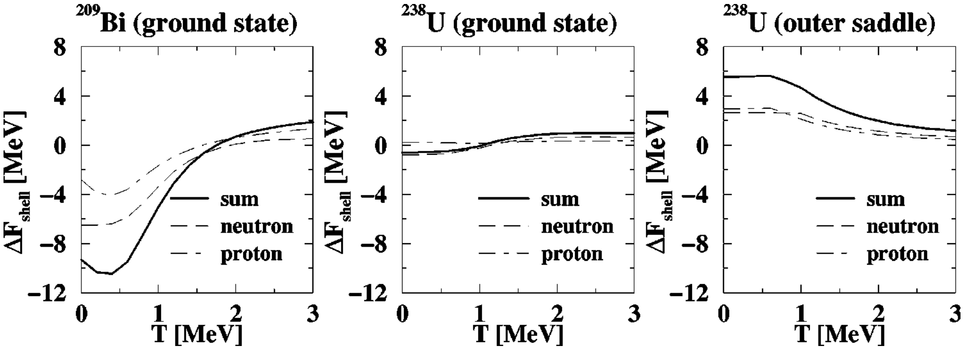

FIG. 6. The shell-plus-pairing correction to the free energy as a function of temperature for ^{209}Bi, ^{238}U in their ground states and for ^{238}U at the symmetric outer saddle-point deformation. The deformations are kept constant in the calculations and correspond to the zero temperature ground states and saddle point.

$$E_{LDM}=-a_1\left[1-\kappa\left(\frac{N-Z}{A}\right)^2\right]A+a_2\left[1-\kappa\left(\frac{N-Z}{A}\right)^2\right]$$
$$\times A^{2/3}f(\text{shape})+\frac{3}{5}\frac{e^2}{r_0}\frac{Z^2}{A^{1/3}}g(\text{shape})$$
$$-\frac{\pi^2}{2}\frac{e^2}{r_0}\left(\frac{d}{r_0}\right)^2\frac{Z^2}{A}+\delta. \tag{35}$$

This expression has four adjustable parameters a_1, a_2, κ, and r_0. The revised parameter set of Ref. [29] is used in the calculations:

$$a_1=15.4941 \text{ MeV}, \tag{36}$$

$$a_2=17.9439 \text{ MeV}, \tag{37}$$

$$\kappa=1.7826, \tag{38}$$

$$r_0=1.2249 \text{ fm}. \tag{39}$$

The first term represents the volume energy. The second term denotes the surface energy. The ratio of the surface area at an arbitrary deformation to the original sphere is given by the function $f(\text{shape})$. The Coulomb energy can be found in the third term. The function $g(\text{shape})$ is the dimensionless ratio of the electrostatic energy of a distorted sharp distribution to that of a sphere. The fourth term corrects for the diffuseness of the charge distribution. The surface-thickness parameter d equals 0.5461 fm. Finally, the fifth term contains the pairing effect. The pairing term δ equals $-11/\sqrt{A}$, 0, $11/\sqrt{A}$, for even-even, even-odd, and odd-odd nuclei, respectively.

A consistent generalization of the Strutinsky method comprising excitation requires a LDM that is able to describe a heated liquid drop. If a nucleus is excited, the volume and surface area increase, while the density $n(T)$ and the surface tension $\sigma(T)$ decrease. Hasse and Stocker [30] have introduced temperature effects into a LDM by computing the temperature-dependent behavior of the nuclear density and the surface tension:

$$n(T)=n(0)(1-\alpha T^2), \quad \alpha=0.0032 \text{ MeV}^{-2}$$

$$\sigma(T)=\sigma(0)(1-\beta T^2), \quad \beta=0.0114 \text{ MeV}^{-2}. \tag{40}$$

The volume term, for instance, will scale with the change in the nuclear density. Following this line of thought, several scaling laws can be derived. The temperature dependence of the volume, surface, and Coulomb part of the LDM free energy becomes, according to Stocker [31],

$$F_{vol}^{LDM}(T)=E_{vol}^{LDM}(0)\frac{n(0)}{n(T)}\approx E_{vol}^{LDM}(0)(1+\alpha T^2), \tag{41}$$

$$F_{surf}^{LDM}(\text{def},T)=E_{surf}^{LDM}(\text{def},0)\frac{\sigma(T)}{\sigma(0)}\left(\frac{n(0)}{n(T)}\right)^{2/3}$$
$$\approx E_{surf}^{LDM}(\text{def},0)\left[1-\left(\beta-\frac{2}{3}\alpha\right)T^2\right], \tag{42}$$

$$F_{Coul}^{LDM}(\text{def},T)=E_{Coul}^{LDM}(\text{def},0)\left(\frac{n(T)}{n(0)}\right)^{1/3}$$
$$\approx E_{Coul}^{LDM}(\text{def},0)\left(1-\frac{1}{3}\alpha T^2\right). \tag{43}$$

The volume term of the free energy depends on temperature but not on deformation. Hence the free deformation energy for the isothermal process, normalized to zero for the spherical shape, becomes

$$F_{\text{def}}^{LDM}(\text{def},T)=F^{LDM}(\text{def},T)-F^{LDM}(\text{spherical},T)$$
$$=E_{surf}^{LDM}(\text{def},0)\left[1-\left(\beta-\frac{2}{3}\alpha\right)T^2\right]$$
$$+E_{Coul}^{LDM}(\text{def},0)\left(1-\frac{1}{3}\alpha T^2\right). \tag{44}$$

Since $\beta>\alpha$, the isothermal LDM barrier is lowered when the temperature rises.

An alternative for this LDM could be the Yukawa-plus-exponential model by Krappe, Nix, and Sierk [32] (or finite range model), which is generally believed to give more realistic deformation energies. However, the ALICE-91 outcomes in Sec. III C suggest a preference for the rotating-liquid-drop model (RLDM) over the rotating finite range model (RFRM) by Sierk [33] in the calculation of the fission cross sections, and, in addition, the barrier heights obtained with the Myers and Swiatecki LDM are in excellent agreement with those of the RLDM in ALICE-91 in the mass region of interest in this paper (see Fig. 10). Therefore from the viewpoint of consistency between the Brosa and the ALICE-91 calculations the use of the LDM by Myers and Swiatecki is preferred. Furthermore, no proof exists that the finite range model would perform better at higher temperatures, or would yield better results with respect to the fragment masses. In a recent paper by Möller and Iwamoto [21] zero-temperature saddle-point shapes are investigated with the Yukawa-plus-exponential model. No final fission fragment masses are predicted, but the value for the average heavy fragment for ^{232}Th at the outer saddle point is determined to be $A_h=134.6$, and compared to the experimental value of the final average heavy fragment mass of $A_h=139.5$ [34]. Our approach yields a prescission shape for the standard I mode in ^{232}Th with $A_h=137.2$ (for zero temperature).

Möller and Iwamoto [21] also include a shape-dependent Wigner term in their calculations, which lacks here. The contribution to the barrier height by the shape-dependent part is around 1–2 MeV [35] which is of the same order of magnitude as the uncertainty in the shell correction calculation of 1

MeV. The precise influence of this term on the determination of the prescission shapes is not yet known.

B. Search for fission channels

The five deformation parameters from Eq. (5) and the corresponding deformation energy induce a search in a six-dimensional space for the paths that follow a minimal deformation energy. This is a difficult task. Minimizing the deformation energy without restrictions on the parameters will reveal the position of the ground state, the end of a fission channel, and perhaps a local second minimum in between an inner and outer barrier. The outcome depends heavily on the starting point of the minimization procedure. Saddle points at the top of the barriers and points connecting the minima with these saddle points remain invisible.

Apart from the ground state and second minima, which can be found easily, other points in the deformation space are needed to find the full fission channel. In order to know where to look for the fission modes in deformation space, a stroll through a subspace spanned by the parameters l, r, and z is made. The nucleus is once more described by the Lawrence parametrization of Eq. (4), which is now truncated at $N=2$. This approximation of the detailed nuclear shape is of course less accurate than with five parameters. The outcome, however, will mainly serve as a first guess for the final calculation. The subspace is investigated in several slices, located around the so-called Rayleigh criterion [36]. The Rayleigh criterion, applied to the used shape parametrization, relates the total length $2l$ of the prescission shape with the neck radius r:

$$2l=11r. \tag{45}$$

According to derivations by Brosa *et al.* [16] this point marks the onset of instability of the neck against random neck rupture. The four-dimensional subspace can be reduced further by one dimension, if this criterion is used to calculate l from r according to Ref. [37]:

$$l_{offset}=\frac{11}{2}\left(r_{offset}-\frac{\zeta}{2}\right)-\zeta. \tag{46}$$

The slice with offset $\zeta=0$ gathers all points of the subspace for which Eq. (45) is fulfilled. With a positive value of the offset ζ a new slice is created which is moved from the Rayleigh criterion in the direction of the outer saddle point. A negative offset corresponds to deformations which are nearer to the end of the fission channel. The l value is fixed by Eq. (46), and the c and s values are approximated from the definition of curvature and center of mass computed with the truncated Lawrence parametrization. Subsequently, the potential energy can be calculated for each pair of (r,z) at a given offset. In Fig. 7 contour plots are shown for the energy as a function of (r,z) for temperatures and offsets as indicated. Three distinct minima belonging to fission modes can be recognized in these contour plots. They are marked with a circle for the superlong (SL) mode, with a star for the standard I (ST I) and with a triangle for standard II (ST II). The SL mode resides at zero z which means no asymmetry. It is responsible for the symmetric contribution to the fission process. The standard modes lie close to one another. ST II has a somewhat larger asymmetry than ST I, it will lead to the contribution to the mass distribution with the higher average heavy mass. At a temperature of 2.0 MeV, only the SL mode survives, while ST I and ST II have melted away. The resulting values for the deformation parameters form points of support in the final search.

These points of support in deformation space, between which the final search can be performed, come in very handy. They provide a restriction that may be imposed on the ultimate minimization: increasing deformation starting from the ground state. The ratio of l and r is a measure for the deformation. In between two points of support that are characterized by (l,r,z,c,s) and (l',r',z',c',s'), the first guesses for the next channel point $i+1$ to be found are given by

$$\begin{aligned} r_{i+1,g}&=r_{i,f}+\frac{r'-r}{N},\\ z_{i+1,g}&=z_{i,f}+\frac{z'-z}{N},\\ c_{i+1,g}&=c_{i,f}+\frac{c'-c}{N},\\ s_{i+1,g}&=s_{i,f}+\frac{s'-s}{N}. \end{aligned} \tag{47}$$

N is the number of steps to fill the gap between the two existing points of support, and i runs from 0 to N. The subscript g denotes a value used as a first guess, whereas f is linked to the value found in the previous step after minimization with respect to the energy. This recipe of constructing the new guesses makes sure that the search starts at a larger deformation for each new step. The following requirement imposed on the search ensures that this increase in deformation is maintained in each step:

$$l_{i+1,g}=l_{i,f}+\frac{l'-l}{N}=\frac{l_{i,g}}{r_{i,g}}r_{i,f}+\frac{l'-l}{N}. \tag{48}$$

Furthermore, this last condition reduces the deformation space by one dimension.

If the first guess based on the stroll in the four-dimensional subspace is good enough, the search will deliver points belonging to that particular fission mode. The SL and the ST modes are well separated in deformation space. Distinguishing between those modes poses no difficulty at all. Although the ST I and ST II modes lie much closer to each other, in many cases the minimization routine arrives at the right answers. Sometimes, however, a search for ST I results in a point that in reality corresponds to ST II, or vice versa. Fortunately, on the basis of all the deformation parameters together it is possible to decide to which of both standard modes these points belong. In the next sections, the results for the channels found are translated into barrier parameters and prescission shapes.

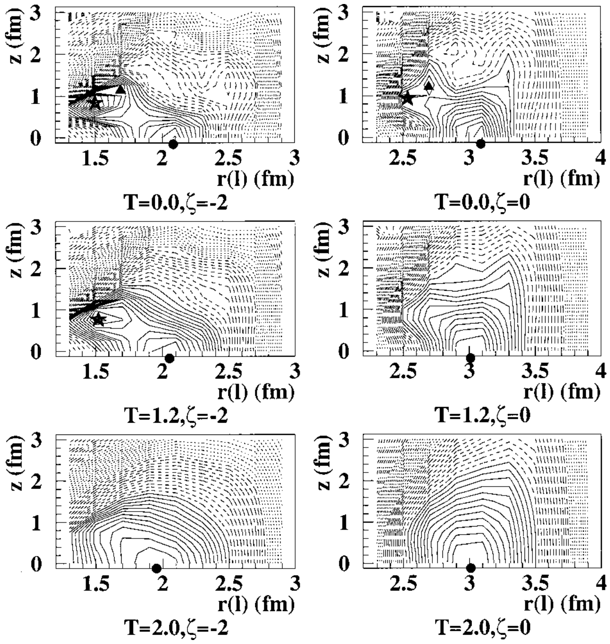

FIG. 7. Contour plots for ^{230}Th at different temperatures T and deformation subspaces denoted by ζ. The contours connect points in the (r,z) plane with the same deformation energy. Minima in these plots mark the position of fission channels. The circles correspond to the superlong (SL) mode, stars to standard I (ST I), and triangles to standard II (ST II).

Möller and Iwamoto [21] propose a new method to determine saddle-point shapes by fully exploring all deformation space accessible. Unfortunately, such an approach could not be adopted here because of the large number of nuclides and temperatures needed for this work and the corresponding enormous amount of computing time.

C. Investigated nuclides and temperatures

Since the fission channel searches are very time consuming, the computational costs have to be reduced considerably. This is achieved by cutting the number of nuclides as well as the number of temperatures. The searches are performed at the following temperature grid:

$$0.0,\ 0.3,\ 0.6,\ 0.9,\ 1.2,\ 1.6,\ 2.0,\ 2.5,\ \text{and}\ 3.0\ \text{MeV}.$$

Quantities such as the prescission shapes and the barrier parameters turn out to behave smoothly enough to make the interpolation between these energy points meaningful. These interpolations are necessary whenever the information at any arbitrary temperature has to be obtained. Equation (40) used to compute the LDM energy is only guaranteed to be valid up to a temperature of 2.0 MeV, which corresponds to an excitation energy of approximately 120 MeV. Nevertheless, fission channel searches are performed up to $T = 3.0$ MeV, because the model has to be used to describe experiments up to about 200 MeV. The final mass distributions computed at these high energies will judge the validity of this assumption.

The number of studied isotopes is also restricted. In order to be able to describe nucleon-induced fission reactions up to 200 MeV, the investigated nuclides populate the valley of stability and the neutron-deficient region, see Fig. 8. Again, interpolation is used to fill in the gaps.

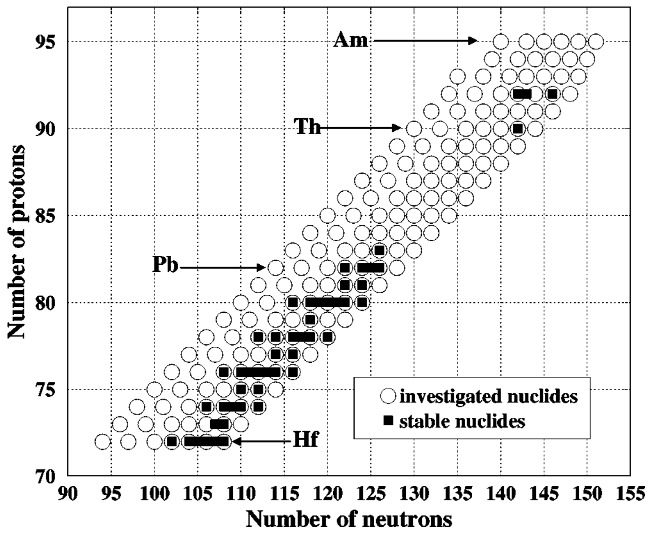

FIG. 8. The location of the nuclides at the chart of nuclides investigated for the determination of the barrier parameters and the prescission shapes as a function of temperature.

D. Fission barriers

In Fig. 9, the LDM deformation energy for ^{238}U obtained from a channel search is depicted as a function of the distance between the centroids of the fragments d. The calculation has been performed for several temperatures. The resulting barrier is single-humped and decreases in height with increasing values of the temperature. Only one (symmetric) fission mode exists if no shell effects are taken into account. Temperature zero LDM fission barrier heights for beta-stable nuclei as a function of nuclear mass can be found in Fig. 10. A comparison is made with the values obtained with the

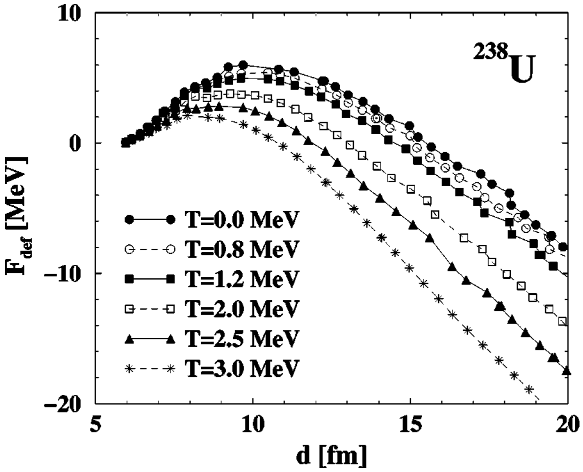

FIG. 9. LDM deformation energy as a function of d, the distance between the fragment centers and for several values of the temperatures T.

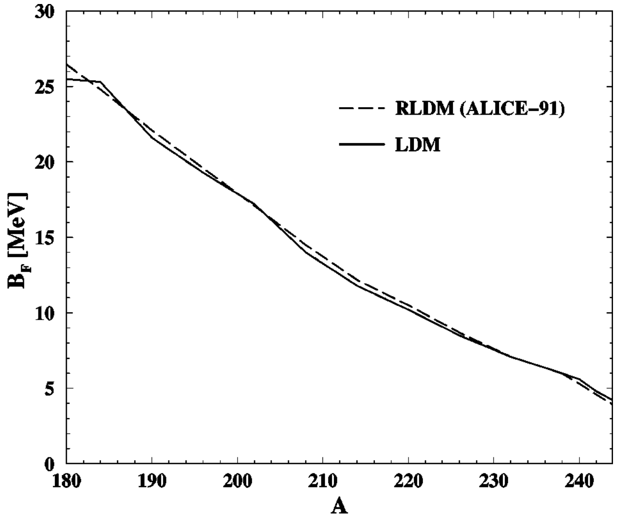

FIG. 10. LDM fission barrier heights for beta-stable nuclei as a function of nuclear mass for $T=0$ MeV, and compared to the values obtained with a rotating-liquid-drop model from the code ALICE-91.

rotating-liquid-drop model (RLDM) incorporated in the code ALICE-91 [38]. The agreement is consistent throughout the whole mass region within 0.5 MeV.

Introducing the shell effects changes the barrier drastically. This is illustrated in Fig. 11. The upper part shows the double-humped barrier of the SL fission mode in ^{238}U for $T=0.0$ MeV. The middle and lower panels contain the decomposition of the deformation energy into the LDM energy and the shell correction term. The shell correction has alternating positive and negative values with deformation. This gives rise to the split of the single-humped LDM barrier.

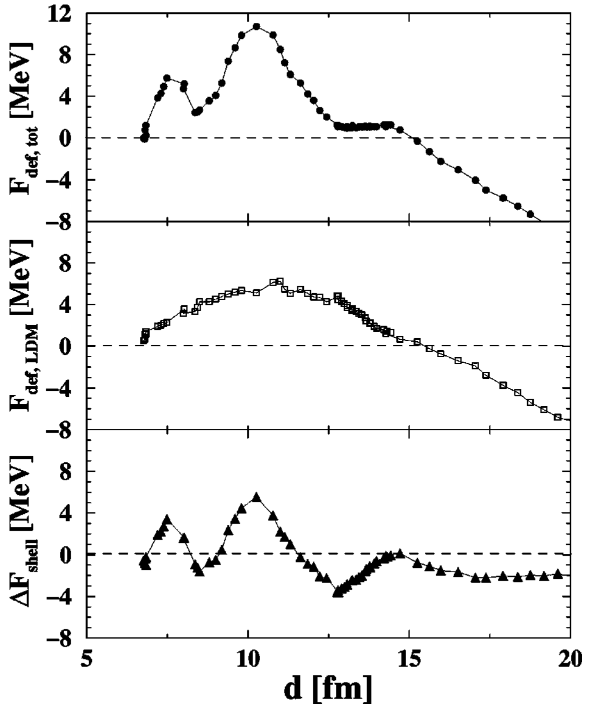

FIG. 11. Decomposition of the deformation energy of the SL mode in ^{238}U into the LDM energy and the shell correction for $T=0.0$ MeV.

Moreover, shell corrections are responsible for the existence of other fission modes than only a symmetric mode. In Fig. 12 the three dominant fission channels for ^{238}U are plotted as a function of d for different temperatures. At low temperatures, all three fission modes are present. They seem to have the first inner barrier in common and to bifurcate in the second minimum. The outer barrier is lowest and narrowest for ST I, making this the strongest mode. The SL and ST II outer barriers have a comparable height, but the SL width is larger. Hence the transmission through the ST II barrier is larger than through the SL barrier for subbarrier excitation energies. With an increase in temperature the shell effects melt. First, the distinction between the two asymmetric standard modes disappears, before at even higher excitation energies the standard mode and double-humped structure vanish altogether. Above $T=2.0$ MeV only the liquid drop barrier remains, resulting in symmetric fission. Figure 13 is the equivalent picture for ^{208}Pb. Only one standard mode is present and the shape of the outer barriers is completely different. Again the inner barrier is shared by both fission modes. The symmetric fission barrier is the lowest for all temperatures.

In order to determine the relative weight of the different fission modes, the barrier heights and widths must be extracted from the channel calculations. This is done by fitting a parabola to the barriers:

$$F_{\mathrm{def}}=-\frac{1}{2}C(d-d_{top})^2+B_F,$$

$$\hbar\omega=\hbar\sqrt{\frac{C}{m}}. \qquad (49)$$

B_F is the barrier height in MeV and d_{top} gives the position of the barrier top in fm. The curvature $\hbar\omega$ in MeV is given by the fitting constant C in MeV/fm^2, Plank's constant $\hbar$ in MeV's, and the ground-state nuclear mass m in MeV s^2/fm^2. A small value of the curvature corresponds to a broad barrier and vice versa. In this manner, a set of barrier parameters is obtained for each nucleus at a given temperature.

1. Behavior of barrier parameters

In Fig. 14 the barrier heights of the different fission modes are plotted for beta-stable nuclei at $T=0.0$ MeV. If no stable nucleus exists, the one with the longest half-life is taken. In the actinide region the barriers are much lower, which demonstrates the higher fission cross sections for these nuclides. Between lead and actinium there is a rapid decrease in the barrier height. Subactinides do not possess a standard II mode. The SL mode in this region clearly has the lowest barriers, making symmetric fission dominant. The SL fission barrier height in the very neutron-deficient region, which is generally lower, is included as well. In these calculations, nuclei with about ten neutrons less than the beta-stable nuclei have been chosen. Figure 15 contains the fission barrier widths for the nuclei in the valley of stability.

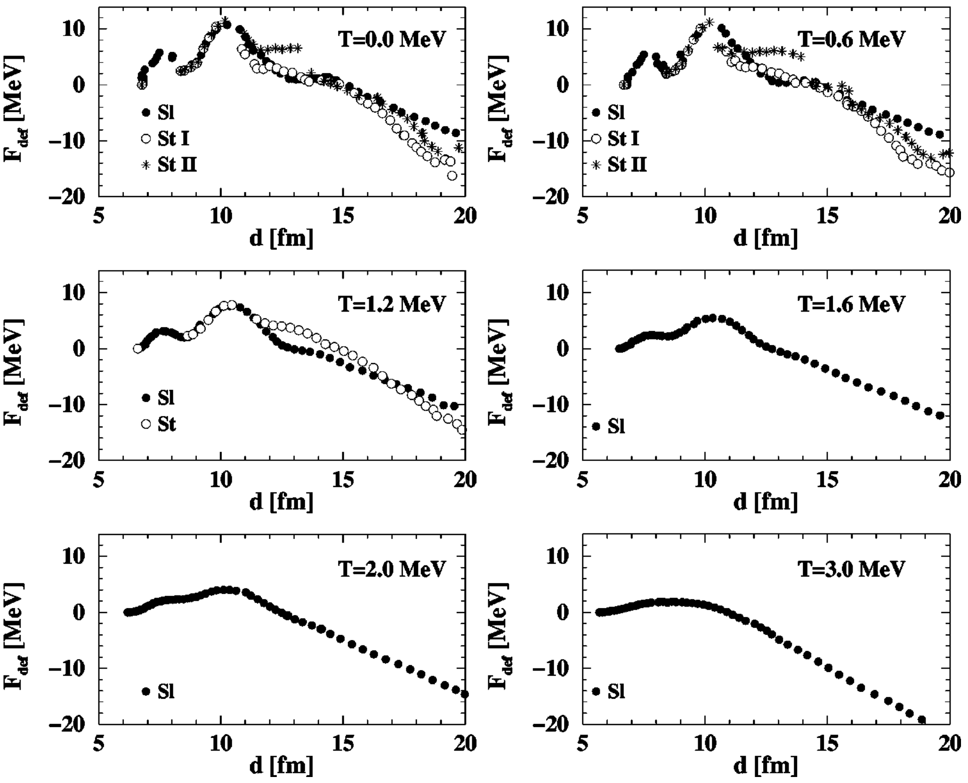

FIG. 12. SL, ST I, and ST II fission channels at varying temperatures for ^{238}U.

For subactinide nuclei the width cannot be obtained by fitting a parabola, because of the deviating shapes. Therefore the curvatures are only shown for the heavier nuclides. In the actinide region, the standard fission mode exhibits the highest curvatures and hence the narrowest barriers.

Another interesting result concerns the behavior of the fission barrier heights for different isotopes of an element. This can be found in Fig. 16. The superlong and the standard I barrier heights are collected for plutonium, actinium, astatine, and lead. Starting at the line of stability on the right-hand side of these plots, the barrier height changes in going to the neutron-deficient isotopes on the left. In the actinide region, the barrier height of neutron-poor nuclides is slightly smaller. This effect is related to a decrease in the surface term in the potential, thereby increasing the influence of the Coulomb force (see Fig. 14). On the edge of the actinide region, however, the barrier first drops and, subsequently, increases. This is coupled to the steep increase of the barrier height when leaving the actinide region (see Fig. 14). Furthermore, ^{215}Ac possesses a closed neutron shell ($N=126$),

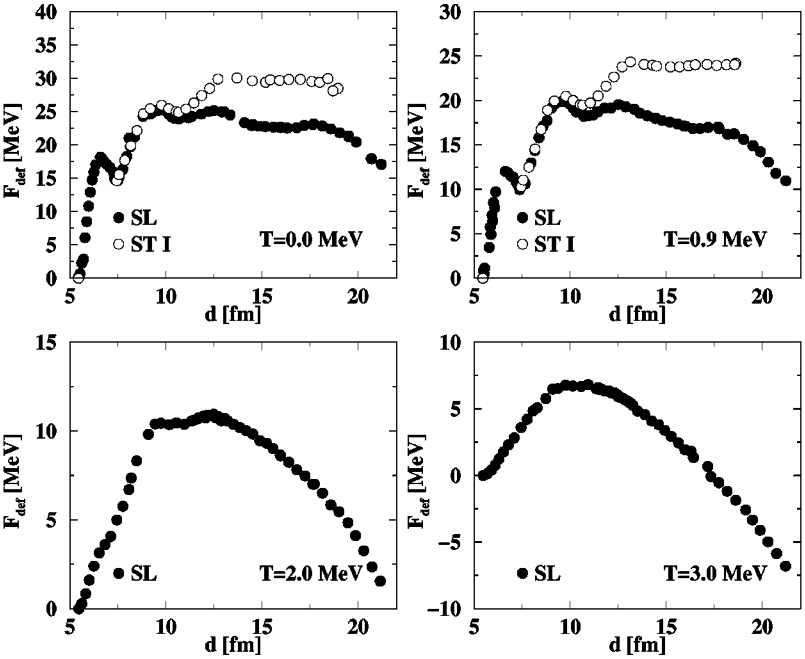

FIG. 13. SL and ST I fission channels at varying temperatures for ^{208}Pb.

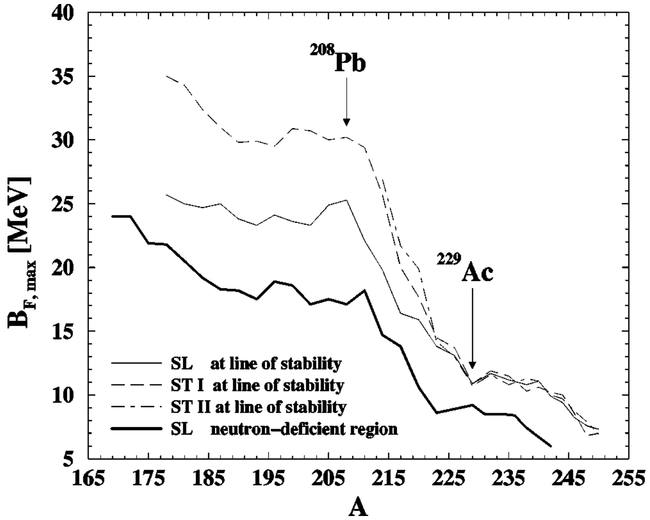

FIG. 14. SL, ST I, and ST II barrier heights for the beta-stable nuclei. The SL fission barrier height in the very neutron-deficient region (i.e., nuclei with about ten neutrons less than the beta-stable nuclei) is included as well. All values are for $T=0.0$ MeV.

which is linked to a higher barrier as well. In the transition region between lead and actinium, there is a competition between all these effects that is also observed for actinium and plutonium. Barrier heights increase at first and tend to decrease for the very neutron-deficient nuclides. The maxima coincide with ^{208}Pb and ^{211}At, which possess just like ^{215}Ac the same closed neutron shell ($N=126$). Arriving in the sub-actinide area around lead, the behavior of the actinide region is recovered: barriers are dropping with a smaller neutron number. Another visible feature is the general decrease in barrier height with an increase in temperature, which has been encountered earlier in other results as well.

2. Comparison to experimental barrier parameters

Transmission through a fission barrier is given by two ingredients: the level density and the penetrability through the barrier. An expression for the penetrability through a parabolic fission barrier has been derived by Hill and Wheeler in terms of the barrier height and the curvature as defined in Eq. (49). These concepts will be further introduced in the next section.

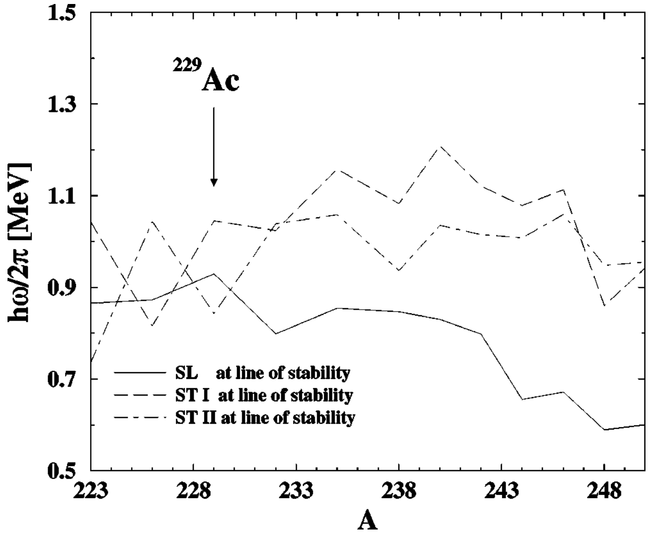

FIG. 15. Fission barrier curvatures of heavy nuclei at line of stability. All values are for $T=0.0$ MeV.

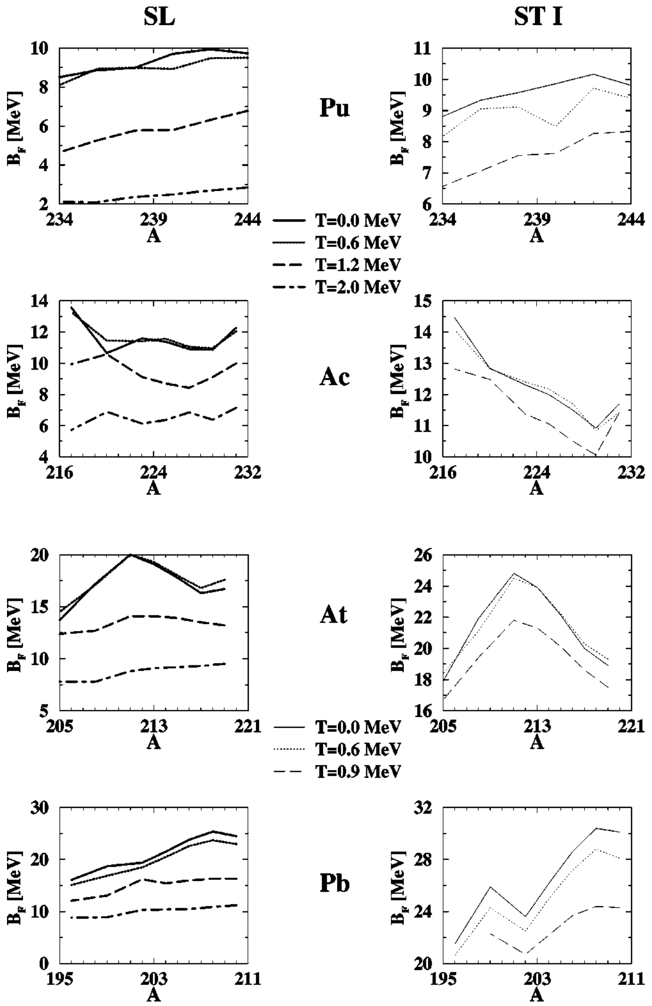

FIG. 16. SL and ST I fission barrier heights as a function of the nuclear mass for Pu, Ac, At, and Pb isotopes.

Based on certain assumptions on the level density, it is possible to extract from experimental fission cross sections as a function of energy the barrier parameters, by making a fit of the transmission through a double-humped barrier. Moreover the assumption is usually made that one (asymmetric) fission mode is dominant. This corresponds, in most cases, to the lowest outer barrier. A famous collection of experimental barrier parameters has been obtained by Bjørnholm and Lynn [39]. Another collection has been made by Maslov [40]. In Table I the experimental barrier heights and widths of both data compilations are compared to the outcomes of the theory for the inner barriers. The theoretical results agree better with the data taken from Ref. [39]. For most nuclei the calculated height is somewhat larger than the experimental value. The average deviation is approximately 0.5 MeV. The curvatures agree very nicely as well. Barrier heights in both data compilations themselves differ also by about 0.5 MeV. This indicates the sensitivity of the fit on

TABLE I. Theoretical fission barrier parameters for the inner barrier, compared to experimentally determined values. The calculations have been performed at $T=0.0$ MeV. The references indicate the sources of the experimental parameters.

	Experiment		Theory		
Nuclide	B_F (MeV)	$\hbar\omega$ (MeV)	B_F (MeV)	$\hbar\omega$ (MeV)	Ref.
^{230}Th	6.1	0.9	3.1	0.8	[40]
^{232}Th	5.8	0.9	4.0	0.8	[40]
^{231}Pa	5.5	1.0	5.0	0.9	[40]
^{233}Pa	5.7	1.0	5.6	0.95	[40]
^{232}U	4.9	0.9	4.9	0.9	[40]
^{234}U	5.6	1.04	5.4	1.07	[39]
	4.8	0.9	5.4	1.07	[40]
^{236}U	5.6	1.04	6.1	1.02	[39]
	5.0	0.9	6.1	1.02	[40]
^{238}U	5.7	1.04	5.7	1.05	[39]
	6.3	1.0	5.7	1.05	[40]
^{236}Np	5.9	0.6	5.6	1.0	[40]
^{238}Np	6.1	0.65	6.2	1.03	[39]
	6.5	0.6	6.2	1.03	[40]
^{238}Pu	5.5	1.04	5.9	1.03	[39]
	5.6	0.9	5.9	1.03	[40]
^{240}Pu	5.6	1.04	6.2	1.04	[39]
	6.05	0.9	6.2	1.04	[40]
^{242}Pu	5.6	1.04	6.1	1.06	[39]
	5.85	0.9	6.1	1.06	[40]
^{244}Pu	5.4	1.04	5.6	1.02	[39]
	5.7	0.9	5.6	1.02	[40]
^{244}Am	6.3	0.65	7.0	0.96	[39]
	6.25	0.7	7.0	0.96	[40]
^{246}Cm	5.7	1.04	6.1	1.04	[39]
	6.0	0.9	6.1	1.04	[40]
^{250}Cf	5.6	1.04	6.8	1.07	[39]

parameters like the level density.

Table II contains the data on the lowest outer barrier. Here a large discrepancy between the theoretical and experimental values is visible. The theoretical barrier heights overestimate the experimental ones with 4–5 MeV. On the other hand, the calculated barrier widths are much larger, indicating narrower barriers. This has always been a shortcoming of the Brosa model, and this outcome lacks a good explanation. Its origin is possibly connected to the shape parametrization with only five deformation parameters. Perhaps the description of the deformed nucleus is good enough up to the first barrier but deteriorates for the more elongated fission shapes. A satisfying answer, however, has not yet been given. Nevertheless, since the outer barriers for all fission modes are much too high, the hope still stands that at least the relative contributions of the different fission modes can be extracted with these theoretical values. This is illustrated in Sec. II H.

TABLE II. Theoretical fission barrier parameters for the lowest asymmetric outer barrier, compared to experimentally determined values. The calculations have been performed at $T=0.0$ MeV. The references indicate the sources of the experimental parameters.

	Experiment		Theory		
Nuclide	B_F (MeV)	$\hbar\omega$ (MeV)	B_F (MeV)	$\hbar\omega$ (MeV)	Ref.
^{230}Th	6.8	0.6	11.6	0.97	[40]
^{232}Th	6.7	0.6	11.9	1.02	[40]
^{231}Pa	5.5	0.5	11.0	1.01	[40]
^{233}Pa	5.8	0.5	12.1	0.98	[40]
^{232}U	5.4	0.6	10.0	0.85	[40]
^{234}U	5.5	0.6	10.8	1.10	[39]
	5.5	0.6	10.8	1.10	[40]
^{236}U	5.5	0.6	11.1	1.06	[39]
	5.67	0.6	11.1	1.06	[40]
^{238}U	5.7	0.6	10.9	1.08	[39]
	5.5	0.6	10.9	1.08	[40]
^{238}Np	6.0	0.45	10.4	1.08	[39]
	5.75	0.4	10.4	1.08	[40]
^{238}Pu	5.0	0.6	9.6	1.07	[39]
	5.1	0.6	9.6	1.07	[40]
^{240}Pu	5.1	0.6	9.9	0.98	[39]
	5.15	0.6	9.9	0.98	[40]
^{242}Pu	5.1	0.6	10.2	1.12	[39]
	5.05	0.6	10.2	1.12	[40]
^{244}Pu	5.0	0.6	9.0	0.96	[39]
	4.85	0.6	9.0	0.96	[40]
^{244}Am	5.4	0.45	9.8	0.85	[39]
	5.9	0.53	9.8	0.85	[40]

E. Weight of fission modes

The three fission modes discussed so far are the only dominant modes for the majority of nuclides. The different barrier characteristics give rise to a separate fission probability along the various fission paths. Obviously, the superlong fission probability plus the standard I and standard II fission probability should add up to the total fission probability. Each mode has its own contribution to the observables of the fission process. The final distributions of the fission-fragment properties (e.g., mass, charge, and TKE) are a superposition of the different distributions stemming from the various fission modes. The recipe employed to extract from the fission barrier parameters the relative contribution of each fission mode is described in this section.

First, the textbook version [41] of the transmission through a parabolic fission barrier with temperature-independent barrier parameters is treated. This is needed to clarify the role of the temperature-dependent barriers later on. As has briefly been mentioned in the previous section, Hill and Wheeler [42] have derived an expression for the penetrability through a single barrier with the shape of an inverted parabola:

$$P_F(E)=\frac{1}{1+\exp\left[\frac{2\pi(B_F-E^*)}{\hbar\omega_F}\right]}. \qquad (50)$$

B_F is the barrier maximum, $\hbar\omega_F$ the curvature of Eq. (49), and E^* the excitation energy. At the saddle-point deforma-

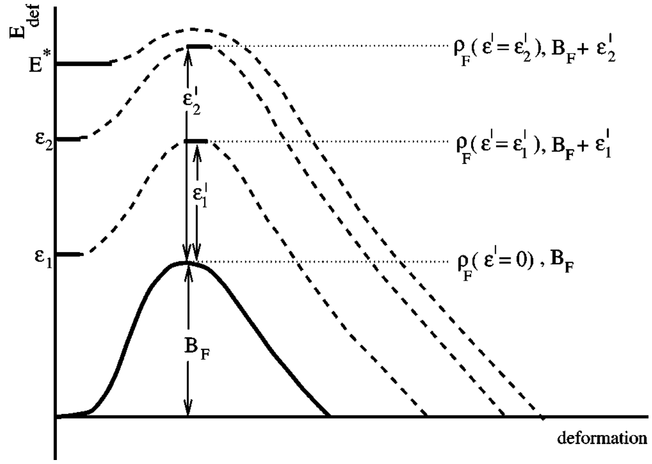

FIG. 17. Use of temperature-independent fission barriers in the determination of the total fission transmission coefficient.

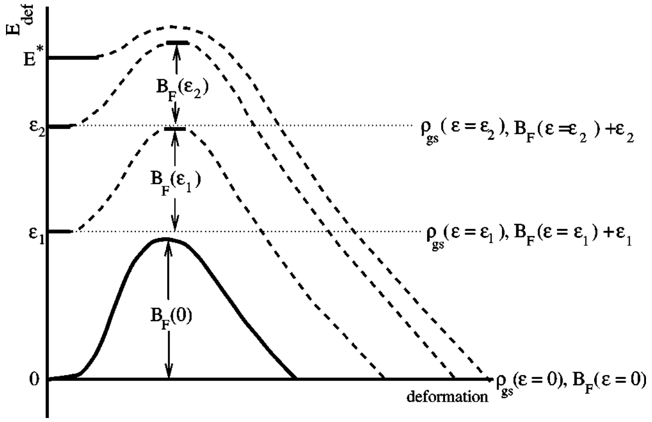

FIG. 18. Use of temperature-dependent fission barriers in the determination of the total fission transmission coefficient.

tion, the nucleus may be in its corresponding ground state, which forms the top of the barrier, or in an excited state. These excited states are called transition states. The fission transmission coefficient not only depends on the penetrability through the ground-state barrier for a given excitation energy, but also through the barriers associated with these transition states, and on the number of transition states available. Neglecting the existence of discrete states on top of the barrier, the density of the transition states enters the description and the expression of the total transmission coefficients becomes

$$\mathrm{Tr}_F(E)=\int_0^\infty d\epsilon'\rho_F(\epsilon')\frac{1}{1+\exp\left[\frac{2\pi(B_F+\epsilon'-E^*)}{\hbar\omega_F}\right]}, \tag{51}$$

with $\rho_F(\epsilon')$ the level density at the saddle-point deformation and an excitation energy ϵ' above the barrier. The level density used here is generally given by

$$\rho(\epsilon)=K_{rot}K_{vib}\rho_{int}(\epsilon). \tag{52}$$

K_{rot} and K_{vib} are the factors describing the rotational and vibrational enhancement of the level density belonging to the noncollective internal nuclear excitations $\rho_{int}(\epsilon)$.

In Fig. 17 the physical meaning of Eq. (51) is illustrated. The contribution for $\epsilon'=0$ is given by $\rho_F(0)=1$ and the penetrability through a barrier characterized by $(B_F,\ \hbar\omega_F)$ with an excitation energy E^*. The contribution for $\epsilon'=\epsilon_1'$ is expressed in terms of $\rho_F(\epsilon_1')$ and the penetrability through a barrier $(B_F+\epsilon_1',\ \hbar\omega_F)$ with the same excitation excitation energy E^*. On top of the ground-state barrier at each excited state ϵ_i' effectively another barrier is built with a height $B_F+\epsilon_i'$ and the width of the ground-state barrier $\hbar\omega_F$. Here the assumption implicitly made is that the widths do not change as a function of excitation energy. From figures like Fig. 12 it can be concluded that this does not hold. Fortunately, this approximation works quite nicely because of the following reason. As long as the shell corrections are present to their full extent, the barrier heights and widths do not change drastically. This means that up to a temperature of ~1.0 MeV (or an excitation energy of ~30 MeV), the barriers constructed at the transition states do resemble the ground-state barrier closely. At high energies, the major contribution to the transmission coefficient arises from the terms in the integral with $B_F+\epsilon'<E^*$, for which the penetrability is close to 1.0. The penetrability for the terms with $B_F+\epsilon'>E^*$ drops below 1.0 so fast that this contribution may be neglected at higher excitation energies.

The choice to introduce temperature-dependent barriers has a different reason than the introduction of temperature-dependent widths. Within the framework of temperature-dependent barriers it becomes relatively easy to describe the vanishing asymmetric fission at high temperatures, since all these phenomena have become linked to the properties of the barriers. If asymmetric fission no longer plays a role this comes out naturally. In this case, the standard barriers and prescission shapes (see next section) become equal to those of the superlong mode, which results in symmetric contributions to all fission-fragment properties. If only zero-temperature fission barriers are used, the information on the melting of fission modes and their disappearance as a function of T should be incorporated into the level density at the saddle deformation. The preference for temperature-dependence of the barriers finds its root in the availability of the original Brosa model, which could be extended with temperature. With temperature-dependent barrier heights and widths, the total transmission coefficient becomes

$$\mathrm{Tr}_F(E)=\int_0^\infty d\epsilon\,\rho_{gs}(\epsilon)\frac{1}{1+\exp\left[\frac{2\pi\{B_F(T(\epsilon))+\epsilon-E^*\}}{\hbar\omega_F(T(\epsilon))}\right]}. \tag{53}$$

Two main differences with Eq. (51) immediately strike the eye: the use of the ground-state level density and the temperature-dependent barrier heights and widths. In Fig. 18 a schematical drawing elucidates the use of Eq. (53). The contribution to Eq. (53) for $\epsilon=0$ is given by $\rho_{gs}(0)=1$ and the penetrability through a barrier characterized by $\{B_F(T(0)),\ \hbar\omega_F(T(0))\}$ with an excitation energy E^*. The contribution for $\epsilon=\epsilon_1$ is given by $\rho_{gs}(\epsilon_1)$ and the penetrability through a barrier $\{B_F(T(\epsilon_1))+\epsilon_1,\ \hbar\omega_F(T(\epsilon_1))\}$ with the same excitation excitation energy E^*.

For the ground-state level density the expression of Gilbert and Cameron [43] is taken. In this formalism, the excitation energy range is divided in a low-energy part governed by the constant temperature formula and a high-energy part described by the Fermi-gas formula:

$$\rho_{temp}(E)=\frac{1}{\tau}\exp\left[\frac{E-E_0}{\tau}\right] \ \ \forall \ \ E\leqslant E_x, \tag{54}$$

$$\rho_{Fermi}(E)=\frac{\exp(2\sqrt{aE})}{12\sqrt{2}\sigma E(aE)^{1/4}} \ \ \forall \ \ E\geqslant E_x, \tag{55}$$

with σ the spin cutoff factor, and a the level density parameter. The energy parameter E_0 and effective temperature τ can be derived from requiring continuity in the level density and its derivate at the matching point E_x that follows from systematics. The Fermi-gas part is evaluated with the level density parameter by Ignatyuk [44], which takes into account the damping of the shell effects with excitation energy.

A nucleus in a state with excitation energy ϵ_1 has a temperature related to the level density parameter $a_{\text{g.s.}}$ by

$$T(\epsilon_1)=\sqrt{\frac{\epsilon_1}{a_{\text{g.s.}}}}. \tag{56}$$

According to the potential energy calculations the isothermal deformation energy of this nucleus equals $B_F[T(\epsilon_1)]$. In these calculations, all levels with the same temperature $T(\epsilon_1)$ have the same deformation energy. This leads to

$$\rho_{\text{g.s.},int}(\epsilon_1)=\rho_{F,int}(\epsilon_1'). \tag{57}$$

If the contribution of the temperature-dependent width can be neglected and the collective enhancement due to the change in the nuclear moment of inertia from the ground state to the saddle point is not taken into account, both approaches (51) and (53) are equivalent. The use of the ground-state level density has the advantage that it is better known from experiments than the saddle-point level density. The disadvantage is the lack of the collective enhancement in this treatment. However, since only relative contributions of the fission modes will be determined in this manner, not the collective enhancement with respect to the ground state is discarded but the collective enhancement with respect to saddle points of other fission modes. This effect is much smaller.

Instead of one single-humped barrier, the outcomes of the channel calculations show double-humped barriers. If the transmission of the first barrier is denoted by Tr_A and that of the second barrier by Tr_B, the total transmission coefficient is given by [41]

$$\text{Tr}_F=\frac{\text{Tr}_A\,\text{Tr}_B}{\text{Tr}_A+\text{Tr}_B}. \tag{58}$$

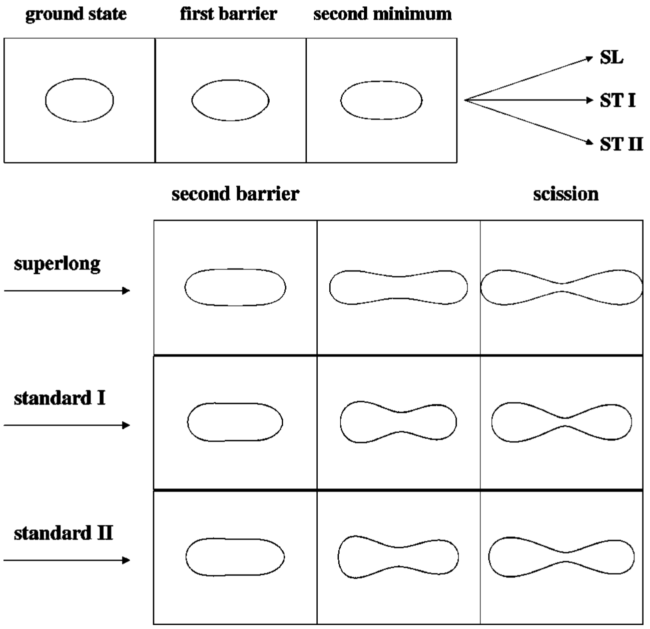

FIG. 19. The evolution of the nuclear shapes of ^{238}U starting in the ground state. In the second minimum the fission path bifurcates into three channels: superlong, standard I, and standard II.

This expression is only valid if at least one of the barriers is lower than the excitation energy, and hence one of the single transmission coefficients is close to unity or greater. For all nuclides considered in this work, the theoretical inner barrier is always much lower than the theoretical outer barriers (see, for example, Table II). In the Appendix is shown why, as a consequence, the relative contributions W of the three fission modes may simply be determined by

$$W_{SL}=\frac{\text{Tr}_{SL,outer}}{\text{Tr}_{SL,outer}+\text{Tr}_{STI,outer}+\text{Tr}_{STII,outer}}, \tag{59}$$

with $\text{Tr}_{SL,outer}$ the transmission coefficient corresponding to the outer superlong barrier evaluated with Eq. (53). Equivalent expressions are valid for ST I and ST II.

F. Prescission shapes

Figures 19 and 20 display the evolution of the nuclear shape between the ground state and the various prescission shapes for ^{238}U and ^{208}Pb. ^{238}U starts in a deformed ground state and elongates further on its way to scission. The characteristic neck of the prescission shapes appears shortly after the outer barrier. The superlong mode does its name credit with its shape that is more elongated than any other fission mode. Furthermore, it results in a symmetric mass division. For the asymmetric modes standard I and standard II the left-hand side contains the heaviest of the two preformed fragments. From the picture it is clear that fission fragments that remain after breaking of the neck will be strongly deformed. The results for ^{208}Pb are fairly similar. The only difference is the spherical ground state.

The parameters that determine the prescission shapes emerging at the end of the fission paths are input for the

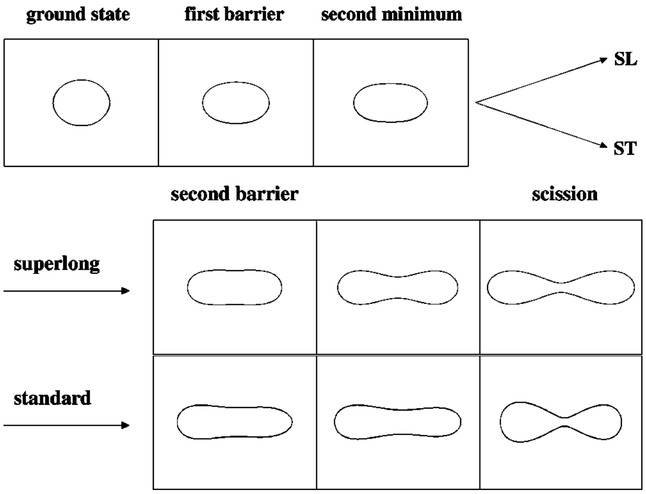

FIG. 20. The evolution of the nuclear shapes of ^{208}Pb starting in the ground state. In the second minimum the fission path bifurcates into two channels: superlong and standard.

RNRM (see Sec. II G), which calculates the fission-fragment properties. These input parameters are the average heavy fragment mass A_h, the half length of the nucleus l and the potential energy of the prescission shape with respect to the ground state. Figures 21 and 22 show results for A_h and l as a function of the neck radius for the three fission modes in ^{217}Ac, ^{231}Ac, ^{226}U, and ^{238}U. The symmetric mode stays around $A_h \approx \frac{1}{2}A$ between ground state and scission. In the second minimum around $r \sim 6$ fm, the standard modes branch off and wander to higher values of A_h. For the neutron-deficient nuclides ^{217}Ac and ^{226}U the difference between ST I and ST II is very pronounced, whereas for the stable nuclides the differences are only a few mass units. From ^{238}U to ^{226}U and from ^{231}Ac to ^{217}Ac, the ST I mode ends at much lower asymmetries, while ST II drops only a few mass units. From Fig. 22 it can be concluded that ST I has a slightly more compact prescission shape than ST II. Again the superlong mode turns out to be the most elongated mode.

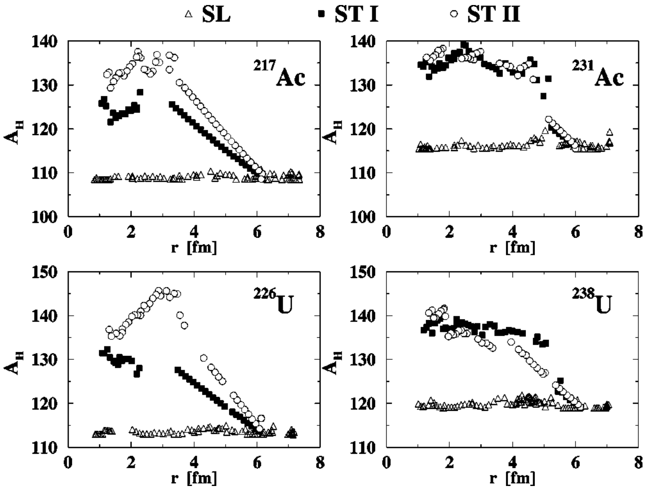

FIG. 21. The average heavy fragment mass for SL, ST I, and ST II as a function of the neck radius r. The nuclides considered are ^{217}Ac, ^{231}Ac, ^{226}U, and ^{238}U. Note that the fission direction in each plot is from the right to the left.

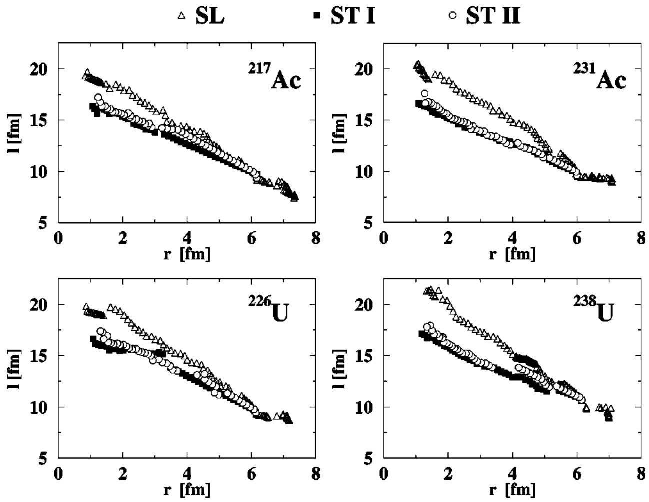

FIG. 22. Half length of the nucleus for SL, ST I, and ST II as a function of the neck radius r. The nuclides considered are ^{217}Ac, ^{231}Ac, ^{226}U, and ^{238}U. Note that the fission direction in each plot is from the right to the left.

According to Brosa [12] the neck becomes unstable against random neck rupture at the Rayleigh criterion, which has already been formulated in Eq. (45). All the deformations beyond this point may therefore contribute to the fission process. The Brosa model gives no clear recipe for the determination of the scission point. It must be situated somewhere between the Rayleigh point and $r \sim 1.2$ fm, which corresponds to a neck size of one nucleon r_0. In order to determine the prescission shapes, an assumption must be made about the exact location of the rupture point in deformation space. Comparison of the model predictions for the mass distributions with several prescission shapes should give the answer. It turns out that the best description is obtained for the standard modes if the prescission shape is chosen at the maximum asymmetry between $r_0 \leqslant r \leqslant 2r_0$. For the SL mode an average value is computed of the A_h and l values obtained in the channel search for $r_0 \leqslant r \leqslant 1.5$ fm, which belongs to a thinner neck.

In Figs. 23 and 24 the A_h and l values are plotted as a function of temperature, again for the nuclides ^{217}Ac, ^{231}Ac, ^{226}U, and ^{238}U. The melting of the fission modes is nicely visible. For higher temperatures the SL mode becomes slightly more compact.

G. Random neck-rupture model

An elaborative description of the RNRM may be found in Ref. [12]. This section merely attempts to communicate its main ideas. In this model, the fission process is regarded as a series of instabilities. After the passage over the barriers, a neck starts to form. If this neck becomes flat its rupture may happen anywhere, which means that the point of future constriction can shift over the neck. This motion of the dent is called the shift instability. The instant that the Rayleigh instability starts to deepen the dent, the position of the asym-

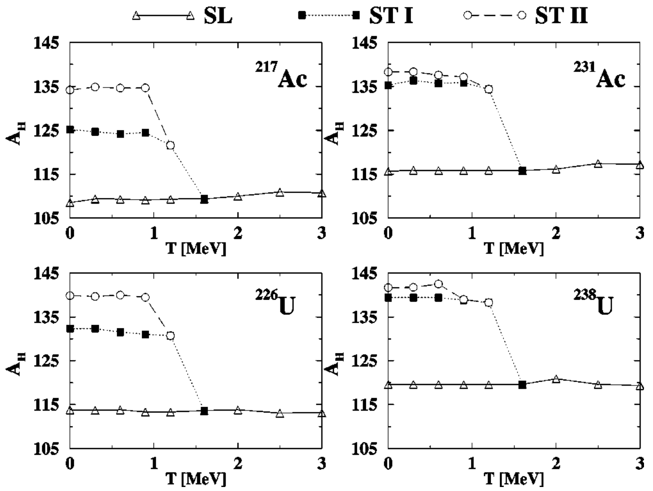

FIG. 23. The average heavy fragment mass of the prescission shape as a function of temperature. The nuclides considered are ^{217}Ac, ^{231}Ac, ^{226}U, and ^{238}U.

metry is frozen and rupture is taking place. The RNRM translates the effects of both mechanisms into measurable quantities.

1. Mass distributions

In order for the shift instability to do its work, a perfectly flat neck is required. The Lawrence parametrization does not meet this need. Hence a new parametrization, the flat-neck representation, is introduced (see Fig. 25):

$$\rho(\zeta)=\begin{cases} (r_1^2-\zeta^2)^{1/2} & -r_1\leqslant\zeta\leqslant\zeta_1 \\ r+a^2c\left[\cosh\left(\dfrac{\zeta-z+l-r_1}{a}\right)-1\right] & \zeta_1\leqslant\zeta\leqslant\zeta_2 \\ [r_2^2-(2l-r_1-r_2-\zeta)^2]^{1/2} & \zeta_2\leqslant\zeta\leqslant 2l-r_1. \end{cases} \tag{60}$$

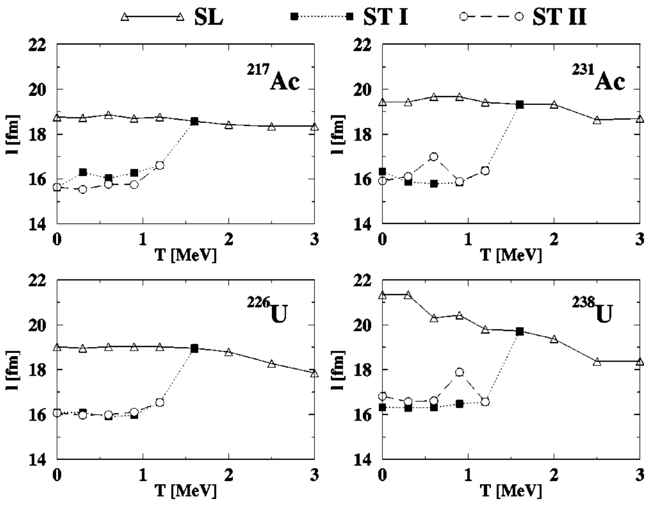

FIG. 24. The prescission shape half length as a function of temperature. The nuclides considered are ^{217}Ac, ^{231}Ac, ^{226}U, and ^{238}U.

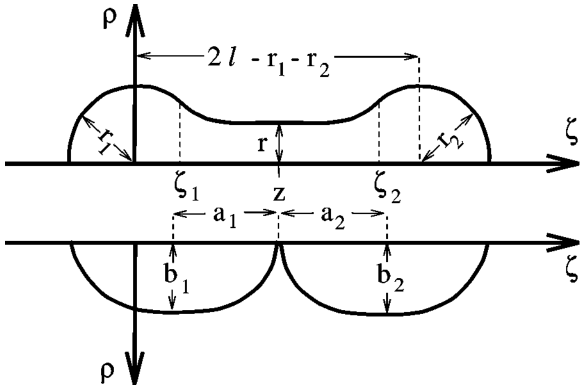

FIG. 25. The upper part illustrates the flat-neck representation. The lower part contains the embedded spheroids parametrization.

The semilength l, the neck radius r, the position z of the dent, and the curvature c are familiar from Eq. (5). The new parameters are: the extension of the neck a, the radii of the spherical heads r_1 and r_2, and the transitional points ζ_1 and ζ_2. By requiring continuity and differentiability of the shape, volume conservation, and a minimal value of c for a really flat neck, only $(l,\ r,\ z)$ remain as independent parameters. Subsequently, the neck radius is eliminated by the Rayleigh criterion. The value of z can be transformed into A_h by Eq. (6). The actual values of A_h and l originate from the channel searches, as mentioned in the previous section.

The last ingredient missing for the computation of the mass distribution is the surface tension:

$$\gamma_0=0.9517\left[1-1.7828\left(\frac{N_{CN}-Z_{CN}}{A_{CN}}\right)^2\right]\ \text{MeV fm}^{-2}. \tag{61}$$

This is taken from the LDM by Myers and Swiatecki [28].

Fluctuations amplified by the shift instability alter the shape slightly and enable the rupture of the nucleus to take place at another point than the most probable point z. In order to determine the fission-fragment mass distribution, the probability of cutting the neck at an arbitrary position z_r has to be calculated. This probability is given by the change in potential energy from z_r to z: $E(z_r)-E(z)$. This is replaced by the energy to cut the nucleus at the two positions: $E_{cut}(z_r)-E_{cut}(z)$, with $E_{cut}(z_r)=2\pi\gamma_0\rho^2(z_r)$. The rupture probability is now proportional to the Boltzmann factor:

$$W(A)\propto\exp\left(\frac{-2\pi\gamma_0[\rho^2(z_r)-\rho^2(z)]}{T}\right). \tag{62}$$

The fragment mass number A can be computed according to the analog of Eq. (6):

$$A(z_r)=\frac{3A_{CN}}{4r_{CN}^3}\int_{-l}^{z_r}\rho^2(\zeta)d\zeta. \tag{63}$$

The theoretical yield is finally determined with the following relation:

$$Y(A)=W(A)+W(A_{CN}-A). \tag{64}$$

In Eq. (62) the temperature of the scissioning nucleus must be provided. All calculations of the PES and the crossing of the fission barriers have been isothermal. However, for the RNRM the loss and gain of excitation energy in crossing the barrier is taken into account into a new excitation energy and temperature at scission:

$$E^*_{scission}=E^*_{\mathrm{g.s.}}+F_{\mathrm{def},scission}. \tag{65}$$

The new excitation energy has two components: the original excitation energy in the ground state $E^*_{\mathrm{g.s.}}$ and the deformation energy at scission $F_{\mathrm{def},scission}$. $F_{\mathrm{def},scission}$ is positive for actinides and becomes negative in the subactinide region. The new excitation energy is related to a new temperature $T_{scission}$ via the level density parameter through Eq. (56). However, a new prescission temperature corresponds to a different prescission shape with a somewhat different value for $F_{\mathrm{def},scission}$. Therefore the temperature $T_{scission}$ has to be determined in a self-consistent manner together with the final prescission shape. If a prescission shape has a high temperature or a very long neck, the mass distribution will be broad. Low temperatures and short necks result in a narrow mass distribution.

2. Post-scission neutron multiplicities

The mass distribution calculated above belongs to the primary fission fragments. Most fragments, however, are highly excited directly after their creation. They take their share of the total excitation energy available at scission given by Eq. (65). Moreover, they are strongly deformed (see, e.g., Fig. 19), which manifests itself in an extra amount of excitation energy set free when this deformation relaxes towards the ground-state deformation of the fragments by the strong surface tension. The superfluous excitation energy is released during the process of postscission neutron and gamma emission. The neutron emission is responsible for a shift of the preneutron emission mass distribution to somewhat smaller masses.

The total excitation energy in a newly created fragment with mass A results from

$$E^*_{fragment}(A)=E_{\mathrm{def},fragment}(A)+\frac{A}{A_{CN}}E^*_{scission}. \tag{66}$$

$E_{\mathrm{def},fragment}(A)$ denotes the deformation energy of the fragment, and the second term contains the portion of the thermal energy at scission of the whole fissioning system picked up by the fragment. The assumption is that the fragment receives a share proportional to its mass.

For the calculation of $E_{\mathrm{def},fragment}(A)$ another shape parametrization is employed: the embedded spheroids (see Fig. 25). The newborn fragments are modeled as two contacting spheroids with major axes a_1 and a_2, which are linked to $2l$ and z_r by

$$a_1=\frac{1}{2}(r_1+z_r),\quad a_2=l-\frac{1}{2}(r_1+z_r). \tag{67}$$

The minor axes b_1 and b_2 follow from volume conservation:

$$b_1^2=\frac{3}{4a_1}\int_{-r_1}^{z_r}\rho^2 d\zeta,\quad b_2^2=\frac{3}{4a_2}\int_{z_r}^{2l-r_1}\rho^2 d\zeta. \tag{68}$$

The energy difference of the spheroidally deformed and the spherical fragment $E_{\mathrm{def},fragment}(A)$ is given by

$$E_{\mathrm{def},fragment}(A,\epsilon)=E^{sph}_{surf}(A)\left(\frac{\arcsin(\epsilon)+\epsilon(1-\epsilon^2)^{1/2}}{2\epsilon(1-\epsilon^2)^{1/6}}-1\right)+E^{sph}_{Coul}(A)\left[\frac{(1-\epsilon^2)^{1/3}}{2\epsilon}\ln\left(\frac{1+\epsilon}{1-\epsilon}\right)-1\right]. \tag{69}$$

The eccentricity is defined as

$$\epsilon_i=\left[1-\left(\frac{b_i}{a_i}\right)^2\right]^{1/2}, \tag{70}$$

and $E^{sph}_{surf}(A)$ and $E^{sph}_{Coul}(A)$ represent the surface and the Coulomb energy of a spherical nucleus.

The neutron multiplicity $\nu(A)$ for a fragment with mass A is now derived by finding the root of the following relation:

$$E^*_{fragment}(A)=\sum_{n=1}^{\nu(A)}(S_n+\eta_n)+E_\gamma. \tag{71}$$

The separation energy S_n is calculated from the mass formula [29]. The average kinetic energy of the neutrons is taken to be $\frac{3}{2}$ times the fragment temperature, and the energy carried off by γ rays E_γ is approximately half the separation energy of the first nonevaporated neutron.

H. Mass distributions in low-energy neutron-induced fission

With the inclusion of temperature effects in the Brosa model, it is now possible to calculate the fission-fragment mass distribution given the excitation energy and the fissioning system. After the calculation of the relative contributions of the three dominant fission modes SL, ST I, and ST II, the mass distributions for all fission modes are determined with the RNRM and, subsequently, added with the proper weight. In the case of low-energy neutron-induced fission the outcome of the model can be compared to experimental data. In this case, the excitation energy is precisely known. It is given by the neutron separation energy of the compound system plus the incoming neutron energy. The influence of multichance fission, i.e., the competition with other reaction channels like particle evaporation, can safely be neglected.

Figure 26 shows preneutron emission mass distributions for low-energy neutron reactions on ^{232}Th, ^{233}U, and ^{238}U. The experimental data are taken from Refs. [45–47]. For all nuclides the ST I mode is the strongest in the predictions. In the case of ^{233}U, it even determines the mass yield curve all by itself. There are three criteria that a predicted mass distribution has to fulfill. First of all the (asymmetric) peaks have to be at the right position. The calculated peak positions for ^{232}Th underestimates the experimental value, but in the case of uranium targets the calculations do very well. Further-

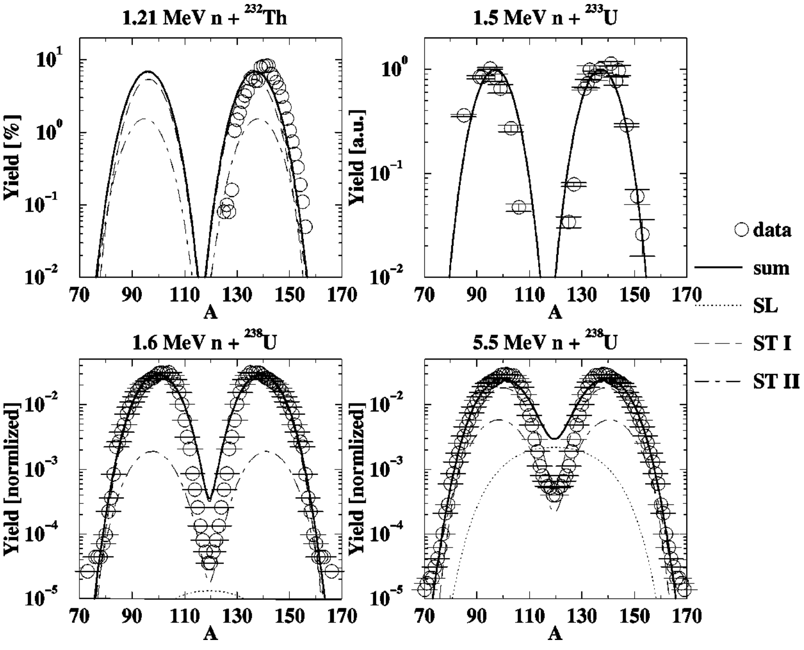

FIG. 26. Preneutron emission mass distributions for low-energy neutrons on ^{232}Th and ^{233,238}U.

more, the widths have to be correct. The outer wings of the experimental distributions are almost reproduced, but the inner wings are not. This may be due to a wrong width. Another possible explanation is a failure in the third criterion: the model has to predict the correct relative share of each fission mode. In the case of 5.5 MeV neutrons on ^{238}U, the symmetric fission portion is clearly overestimated. Probably the competition with neutron evaporation can no longer be discarded at this incoming energy. This would lower the relative contribution of the symmetric fission component as well as the width.

In Fig. 27 some more results are plotted for the heavier nuclides ^{237}Np, ^{242}Pu, and ^{241}Am [48–51]. In general, the reactions on ^{237}Np are described nicely with the model, except the fine structure in the right peak around mass 135. The predictions made for ^{242}Pu and ^{241}Am do not agree with the experimental data in the right hump. The widths are too large and the peak positions are shifted too much to heavy masses. On the other hand, the left wing of the ^{241}Am curve looks somewhat better.

In conclusion, the theoretical mass yield curves for the lighter actinides agree well with experimental data, especially in the asymmetric peak area and the outer wings. In the case of minor actinides, the predictive power is slightly weaker. The overall quality of the prediction of these exclusive fission channels is good enough to justify the implementation of the temperature-dependent Brosa model in analyses at higher energies where only inclusive data are available. To this end, in the next section the process of multichance fission in the nuclear reaction code ALICE-91 is treated in

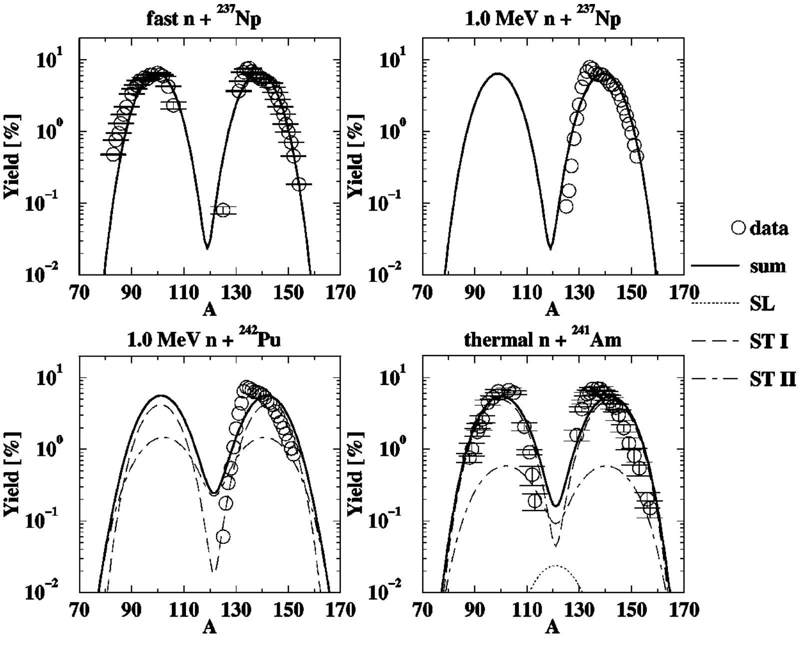

FIG. 27. Preneutron emission mass distributions for low-energy neutrons on ^{237}Np, ^{242}Pu, and ^{241}Am.

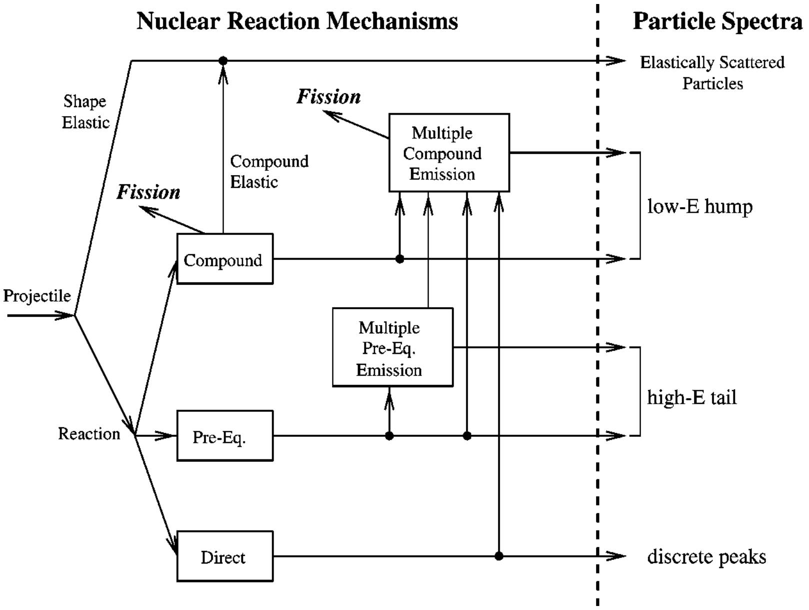

FIG. 28. The role of direct, pre-equilibrium, and compound processes in the description of a nuclear reaction and the outgoing-particle spectra.

detail. This forms the preparation of Sec. IV, in which the connection between ALICE-91 and the temperature-dependent Brosa model is described together with a comparison with experimental data on intermediate-energy fission.

III. MULTICHANCE FISSION

A. Nuclear reactions

It is generally accepted that three different nuclear reaction mechanisms can be distinguished in light particle-induced reactions: direct, pre-equilibrium, and compound. A classification of these mechanisms can be performed on the basis of the reaction time or, equivalently, the number of intranuclear collisions inside the nucleus before emission.

The time scale of direct reactions is linked to the time needed for the projectile to traverse the target nucleus, which amounts to roughly 10^{-22} s. Only one collision of the projectile with a nucleon inside the target precedes the emission. Consequently, a strong correlation between the initial and final state exists. The term direct reactions include processes like inelastic scattering to a discrete state in the nucleus, charge exchange, knock-out, and transfer reactions. Above an incident energy of about 10 MeV, almost all discrete states of the remaining nucleus with a simple structure are excited by direct processes.

The characteristics of compound reactions are in many aspects opposite to those associated with direct mechanisms. Before emission, a lot of intranuclear collisions take place, which distribute the available excitation energy of the compound system homogeneously over all nucleons. In this equilibrated nucleus there is, subsequently, a probability for a single nucleon to collect in several collisions enough energy to escape the nucleus. Naturally, this process is much slower. Time scales vary with incident energy between 10^{-15} s and 10^{-19} s. These intermediate collisions are responsible for the loss of memory about the details of the initial state (apart from energy and angular momentum conservation). Compound mechanisms govern nuclear reactions with incident energies below 10 MeV.

The properties of pre-equilibrium reactions are situated in between those of direct and compound processes. Historically, it comprises one step nonelastic scattering reactions to the continuum as well as multistep emissions from partially equilibrated systems. This occurs if most of the excitation energy is accumulated on one or a few excited particles. The associated time scales range from 10^{-22} s to typically 10^{-18} s. With each extra intranuclear collision, the system gradually loses more of its memory regarding the initial state. Primary pre-equilibrium emission plays an important role above 10 MeV. For incident energies above 50 MeV, including multiple pre-equilibrium into the description of any reaction is crucial. It profoundly marks the feeding of the nuclides, which lose the rest of their energy in the subsequent compound stage of the reaction (with the possibility to fission).

Figure 28 explains the role of these distinct reaction mechanisms during an arbitrary nucleon-induced reaction in a schematic manner. If a projectile collides with an atomic nucleus it may scatter elastically, leaving the nucleus in its ground state, or it can induce a reaction. In the case of a reaction, the direct, pre-equilibrium, and compound mechanisms start to compete in the description of the first emission. At this stage, the compound process has also a contribution to the elastic channel. If after the first emission enough excitation energy remains inside the new nucleus, secondary or, in general, multiple emission will follow. Depending on the progress towards equilibration, this emission will be due to compound processes or to multiple pre-equilibrium followed by compound emission. Fission is a slow and compound process, since it involves a large deformation of the whole nucleus. Hence it will compete with compound emission, as indicated in Fig. 28. First-chance fission occurs in competition with the primary compound emission. Multichance fission stems from the competition with particle emission in the multiple compound process.

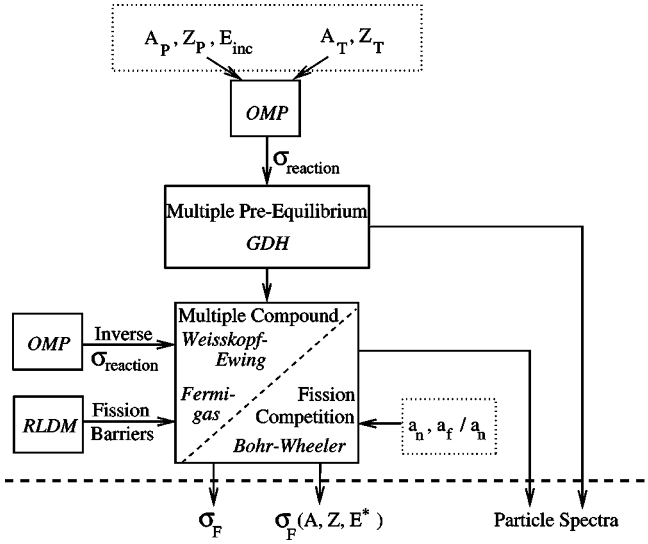

FIG. 29. Basic nuclear models implemented in ALICE-91. User input is indicated by a dotted box.

B. Reaction models in ALICE-91

The nuclear reaction code ALICE-91 [38] has been rather successful in describing nuclear reactions above about 10 MeV [52]. Figure 29 gives the main ingredients of the reaction models implemented in ALICE-91. Since no discrete levels are taken into account in the calculations, the direct reactions are treated effectively by the pre-equilibrium stage. This approximation of the discrete part of the high-energy tail in the spectrum by a continuous spectrum does not alter significantly the prediction for reactions that take place above about 20 MeV. Below these energies the validity of this assumption is questionable. An optical model subroutine (OMP) provides the (inverse) reaction cross sections needed for the overall normalization of all computed cross sections and for the Weisskopf-Ewing compound model (WE). A rotating-liquid-drop model (RLDM) provides the fission barriers that are needed in the Bohr-Wheeler approach to compute the competition between compound emission and fission. The geometry-dependent hybrid model (GDH) [53] describes precompound emission. User input like projectile and target specifications as well as level density parameters is indicated with a dotted box. Of course, a code like ALICE-91 has more options to choose between reaction models or to change basic values, but only the models and the input parameters relevant to this work are treated here. The output of ALICE-91 includes information on the outgoing-particle spectra and the total fission cross section σ_F. Furthermore, ALICE-91 is modified to give also the fission cross section per excitation energy bin of a fissioning nucleus $\sigma_F(A,Z,E^*)$. The total fission cross section is compared to experimental results further on in this section. The quantity $\sigma_F(A,Z,E^*)$ is treated at the end of this section, because it provides the link with the temperature-dependent Brosa model. The physics behind the fission competition with compound decay can be found in the next section.

1. Compound decay with fission competition

In compound decay, the formation and the emission process are completely independent. The WE model makes use of this assumption to describe a reaction from the initial channel α with energy ϵ to the outgoing channel α' with energy ϵ'. The cross section for this reaction can be expressed in terms of a product of the formation cross section of the compound nucleus $\sigma_{c\alpha}(\epsilon)$ and the probability $P_{\alpha'}(\epsilon \to \epsilon')d\epsilon'$ that it will decay into the outgoing channel α' with energy between ϵ' and $\epsilon'+d\epsilon'$:

$$\begin{aligned}\sigma_{\alpha\alpha'}(\epsilon,\epsilon')d\epsilon' &= \sigma_{c\alpha}(\epsilon)P_{\alpha'}(\epsilon\to\epsilon')d\epsilon' \\ &= \sigma_{c\alpha}(\epsilon)\frac{\Gamma_{\alpha'}(\epsilon\to\epsilon')\rho_{\alpha'}(U')d\epsilon'}{\sum_{\alpha''}\int_0^{E-Q''}\Gamma_{\alpha''}(\epsilon\to\epsilon'')\rho_{\alpha''}(U'')d\epsilon''}.\end{aligned} \tag{72}$$

$\Gamma_{\alpha'}(\epsilon\to\epsilon')$ is the width for the decay of the compound system with energy ϵ to a state with emitted energy ϵ' in channel α'. The residual nucleus with excitation energy $U'=\epsilon-\epsilon'-B$ (B is the binding energy of the emitted particle) has a level density $\rho_{\alpha'}(U')$. The Q value of the reaction from channel α to α'' is given by Q''.

With the help of the reciprocity theorem, the cross section to the outgoing channel is linked to that of the inverse reaction:

$$\sigma_{\alpha\alpha'} = \frac{1}{g_\alpha}\frac{\pi}{K_\alpha^2}|S_{\alpha\alpha'}|^2 = \sigma_{c\alpha}\frac{\Gamma_{\alpha'}}{\Gamma}, \tag{73}$$

$$\sigma_{\alpha'\alpha} = \frac{1}{g_{\alpha'}}\frac{\pi}{K_{\alpha'}^2}|S_{\alpha'\alpha}|^2 = \sigma_{c\alpha'}\frac{\Gamma_{\alpha}}{\Gamma}, \tag{74}$$

with K_α the wave number. Reciprocity implies $S_{\alpha\alpha'} = S_{\alpha'\alpha}$. Hence the Weisskopf-Ewing formula arises:

$$\begin{aligned}&\sigma_{\alpha\alpha'}(\epsilon,\epsilon')d\epsilon' \\ &= \sigma_{c\alpha}(\epsilon)\frac{g_{\alpha'}m_{\alpha'}\epsilon'\sigma_{c\alpha'}(\epsilon')\rho_{\alpha'}(U')d\epsilon'}{\sum_{\alpha''} g_{\alpha''}m_{\alpha''}\int_0^{\epsilon-Q''}\epsilon''\sigma_{c\alpha''}(\epsilon'')\rho_{\alpha''}(U'')d\epsilon''},\end{aligned} \tag{75}$$

with $g_\alpha = 2i_\alpha + 1$ the statistical weight of channel α and m_α the corresponding reduced mass. The inverse reaction cross section for formation of the compound nucleus starting from channel α' is identified with the absorption cross section in channel α' resulting from an optical model calculation. The WE approach neglects the spin dependence and is not applicable to reactions to discrete states.

The level densities taken in the WE calculations are of a Fermi-gas type:

$$\rho(E) \propto \frac{\exp(2\sqrt{aE})}{E^{5/4}}. \tag{76}$$

The level density parameter a_n that will be used throughout the evaporation chain has to be given in the input as a constant: $ald = A/a_n$. This implies, that the chosen parameter has to describe in an effective way the expected changes in the level density parameter both with excitation energy and with isotope. Furthermore, as already explained in Sec. II E, the level density in general is constructed from an intrinsic part and rotational plus vibrational factors. By adjusting the level density parameter a_n these collective factors may be effectively taken into account in the intrinsic part given by Eq. (76).

With an expression for the fission probability, the calculation of the competition between compound emission and fission becomes straightforward in the WE formalism. Fission can be simply added as an extra possible outgoing channel. Bohr and Wheeler [54] consider the rate of passage over the single classical fission saddle point. In their approach the fission probability $P_{fission}$ is given by the total state density over all partitions of excitation energy over potential and kinetic energy:

$$P_{fission}(\epsilon)\propto\int_0^{\epsilon-B_F}\rho_F(\epsilon-B_F-\kappa)d\kappa. \tag{77}$$

The level density at the saddle point is denoted by ρ_F. In a classical approach tunneling through the barrier is impossible. Therefore the calculated fission cross section suddenly drops to zero at excitation energies below the barrier height. Equation (77) is equivalent to the transmission coefficient expression through a temperature-independent barrier in Eq. (51), assuming that the penetrability equals 0 for $\epsilon<B_F$ and equals 1 for $\epsilon>B_F$. An important quantity in Eq. (77) is the level density parameter a_f at the saddle point, which is needed to evaluate ρ_F. At the saddle-point deformation the level density parameter is expected to be larger than the ground-state value a_n due to the stronger collective effects as well as a larger intrinsic level density parameter [55]. ALICE-91 requires that the user provides the ratio a_f/a_n as an input. Once more, this value is kept constant throughout the whole evaporation chain. Hence the value given has to represent the effect averaged over all excitation energies and isotopes encountered in the calculation.

In ALICE-91 fission barrier heights and ground-state energies may be supplied by the RLDM by Cohen *et al.* [56] or by the rotating finite range model (RFRM) by Sierk [33]. The RLDM is preferred for the calculations, since it provides a good description for the total fission cross section (see next section). In Fig. 10 the results of this RLDM for beta-stable nuclides is compared to the values obtained with the LDM incorporated in the Brosa model. Barrier heights evaluated in both approaches agree very well. In ALICE-91, the angular momentum dependence of the barrier heights is taken into account. Above a critical value of the angular momentum, the fission barrier vanishes. Moreover, the emitted particles are assumed to decrease the angular momentum.

C. Predictions of fission cross sections

The choice between RLDM and RFRM in the fission calculations is based on results plotted in Fig. 30. The experimental cross sections for neutron-induced fission on ^{232}Th as a function of energy [5] are compared to predictions obtained with the RFRM and the RLDM. The value for the ground-state level density in ALICE-91 has a default value of $a_n=A/9$. There are indications that at high excitation energies this value changes to an asymptotic value of $a_n=A/13$ [57] due to the disappearance of collective effects. Figure 31 shows the effective values assumed in all calculations to be found in this work as a function of incoming projectile energy. Both calculations are carried out with the ground-state to saddle-point level density ratio of 1.00, although the expected value of this ratio is larger than 1.00. The outcome of the RFRM overpredicts the experimental data dramatically at higher energies even with $a_f/a_n=1.0$. A larger level density ratio will only enhance this overprediction, and there is no hope to arrive at a good description of the data by choosing the right level density parameters. The results of the RLDM

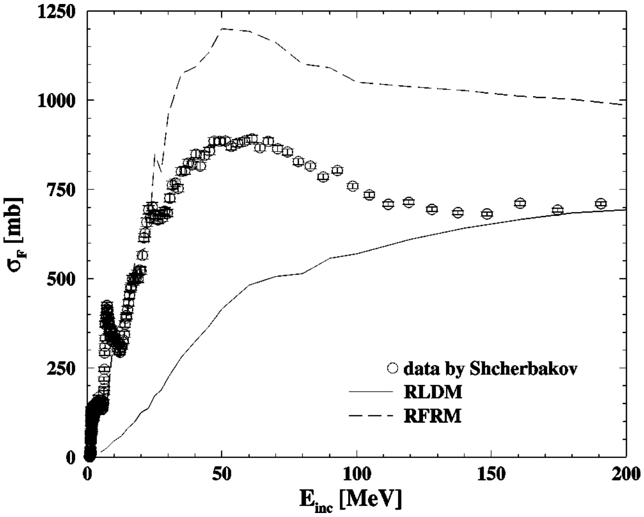

FIG. 30. Experimental fission cross section data for neutron-induced fission on ^{232}Th [5]. ALICE-91 results with the RFRM (dashed line) and the RLDM (solid line) are plotted for comparison.

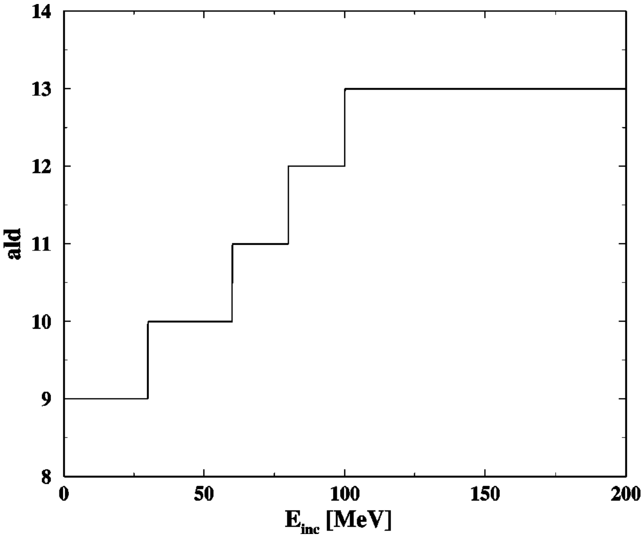

FIG. 31. Values of the ground-state level density parameter $a_n=A/ald$ used in all calculations as a function of incoming projectile energy.

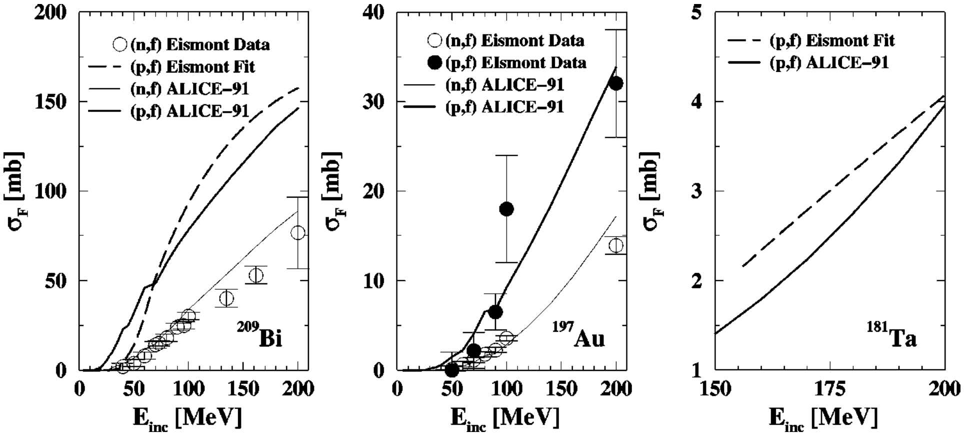

FIG. 32. Experimental fission cross section data compared to ALICE-91 calculations for subactinide targets. All data stem from measurements or from fits to data compilations made by Eismont *et al.* [3,4,58].

are too low, but with a higher value of a_f/a_n a correct answer may be obtained for the fission cross section. This is illustrated next in this section.

The first step in describing fission-fragment mass yields in a satisfactory way consists of predicting the overall normalization. This means that the model should be able to reproduce the total fission cross section. With the RLDM and the ground-state level densities as depicted in Fig. 31 as basic ingredients, it is possible to tune the level density ratio in such a way that the code reproduces both the proton and the neutron-induced fission cross section.

Figure 32 shows results for the subactinide fission cross sections as a function of incoming energy. The experimental fission cross sections are obtained from measurements and data compilations [3,4,58]. The theoretical outcome agrees with the experimental values within 15% for ^{209}Bi and ^{197}Au above 50 MeV in the case of the neutron-induced reactions. Proton-induced fission cross sections may differ by 50% at energies below 70 MeV. The results for ^{181}Ta deviate by about 50%, but the cross sections are one order of magnitude lower than those of ^{197}Au. Two related trends are visible in Fig. 32. First, the fission cross section decreases rapidly with a smaller charge value. Second, the proton-induced fission cross section exceeds the neutron-induced value systematically. This feature is connected to the first observation. In a proton-induced reaction, the average fissioning systems have a slightly higher charge than in a neutron-induced reaction. Consequently, the corresponding total fission cross section is larger.

Comparable results for actinides can be found in Fig. 33. The experimental data on neutron-induced fission are taken from Ref. [5], and the proton data originate from fits to data compilations [58]. By adjusting the level-density ratio to the fission cross section an overall agreement of 10% or better can be achieved. For the nuclides ^{232}Th and ^{238}U a second calculation is included. These results are obtained by fitting the level-density ratio to reproduce the shape of the mass distribution instead of the fission cross section. This is further elucidated in Sec. IV. The outcome of these other calculations lies still within 10% of the proton-induced fission cross section, but overestimates the neutron data with 20 and 15% for ^{232}Th and ^{238}U, respectively.

A comparison of the proton and neutron-induced reactions in Fig. 33 teaches that, in the actinide region, the neutron-induced fission cross section is higher than the proton-induced fission cross section at low energies. At higher energies the situation reverses. Proton reactions possess a threshold around an incoming energy of 10 MeV, because of the Coulomb barrier. Therefore the reaction cross section and thus the fission cross section vanish at incoming

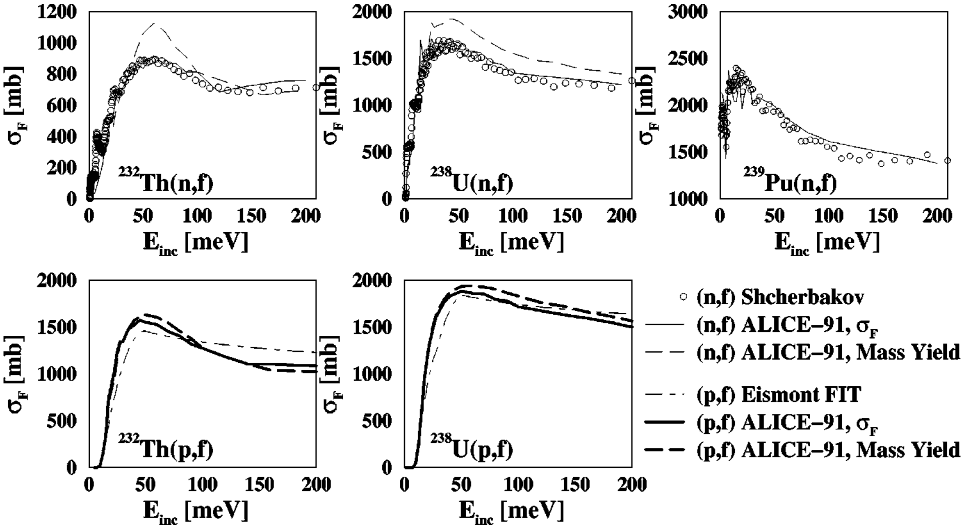

FIG. 33. Experimental fission cross section data compared to ALICE-91 calculations for actinide targets. The neutron-induced fission cross sections, denoted by circles, are taken from Ref. [5] and the proton-induced fission cross sections, denoted by the dot-dashed lines, come from fits to data compilations [58]. Solid lines correspond to calculations tuned to the experimental fission cross sections, while dashed lines are obtained with level-density ratios which give the best agreement with experimental mass distributions in Sec. IV.

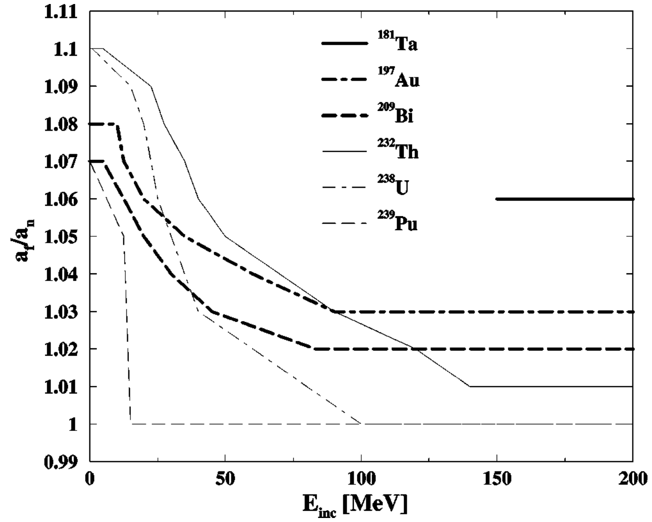

FIG. 34. The saddle-point to ground-state level density ratios a_f/a_n as a function of incoming energy. These values are used to closely describe the experimental data in Figs. 32 and 33.

energies below this threshold. Neutron-induced reactions are not hampered and exhibit already at low energies a sizable fission cross section. At higher energies, this effect no longer plays a role. Here, the difference is again merely determined by the higher charge content in a proton-induced reaction resulting in a larger cross section. This mechanism is exactly the same as in the subactinide region.

The saddle-point to ground-state level density ratios a_f/a_n resulting from the fit to the experimental fission cross sections are plotted in Fig. 34 as a function of incoming energy. In general, the ratio decreases with increasing energies. This is consistent with the picture that at low energies both the collective enhancement and the shell effects, responsible for a change in the intrinsic level density from ground state to saddle point, are strongest. At high excitation energies, roughly above 100 MeV, shell effects wash out and collective effects disappear. Nevertheless, the ratio does not approach 1.0 around 100 MeV incoming energy. This is explained by the fact that the ratio represents an average value which describes effectively all contributions from a variety of fissioning systems at different excitation energies (see next section). Figure 35 contains the level density ratios for ^{232}Th and ^{238}U reproducing the experimental fission cross section as well as the ratios describing the mass distribution shapes. The prediction of the mass distribution requires a larger value of a_f/a_n. The implications of this can be found in the next section.

D. Excitation energy of fissioning systems

The role of different saddle-point to ground-state level density ratios is investigated by looking at the excitation energy distributions of the fissioning systems. A small modification in ALICE-91 makes it possible to extract, apart from the total fission cross section, also the fission cross section as a function of the fissioning isotope and the excitation energy. Figure 36 contains these excitation energy distributions for several isotopes of uranium, protactinium, and thorium in

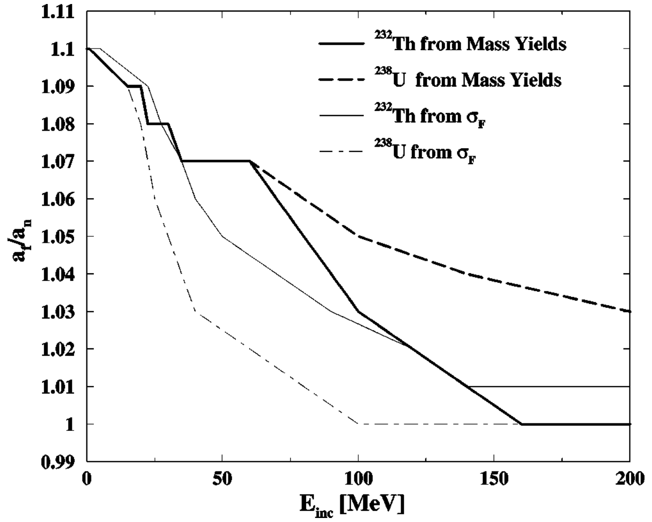

FIG. 35. The saddle-point to ground-state level density ratios a_f/a_n as a function of incoming energy for ^{232}Th and ^{238}U. Both the results tuned to the fission cross sections and those tuned to reproduce the shape of the mass distribution are shown.

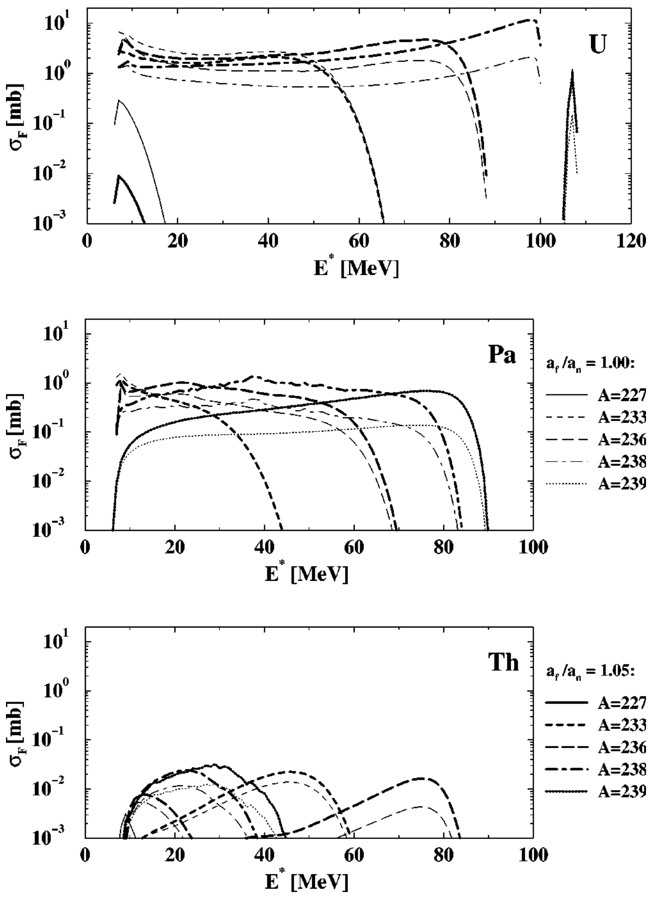

FIG. 36. Excitation energy distributions of the fissioning systems in 100 MeV neutron-induced fission of ^{238}U. The calculation is repeated for two values of the saddle-point to ground-state level density ratio: $a_f/a_n = 1.00$ and 1.05.

100-MeV neutron-induced fission of ^{238}U. The calculation is performed twice; once with $a_f/a_n = 1.00$, which belongs to the best prediction of the fission cross section, and once with $a_f/a_n = 1.05$, which gives the best description of the shape of the fission-fragment mass distribution. From Fig. 36 several conclusions can be drawn. First of all, fission takes place at all possible excitation energies between the maximum excitation energy of the original compound nucleus and the barrier energy. In addition, due to the use of Bohr-Wheeler, fission at subbarrier energies does not contribute, which results in a clearly visible sudden drop at the left-hand sides of Fig. 36. Moreover, fission of isotopes lying further away from the original compound system is characterized by a lower maximal excitation energy coupled to the preceded neutron evaporation. Finally, the contributions from elements with a lower charge drop rapidly.

The role of a_f/a_n also becomes clear by studying Fig. 36. It influences the moment where fission starts predominating particle evaporation. A high value of this ratio means a strong preference for fission over particle evaporation. As can be concluded from Fig. 36, in the case of $a_f/a_n = 1.05$ fission happens earlier in the chain than in the case of $a_f/a_n = 1.00$. This is equivalent to more fission events at higher excitation energies and less fission from very neutron-deficient isotopes.

The link with the temperature-dependent Brosa model is provided by the excitation energy distribution of the fissioning systems. Splitting the total fission cross section into the contribution per excitation energy bin per fissioning isotope enables the calculation of the mass distribution for the specified nucleus (A,Z,E^*) with the correct weight. This will be demonstrated in the next section.

IV. PREDICTIONS OF FISSION-PRODUCT MASS YIELDS

A. Coupling of temperature-dependent Brosa model with ALICE

In combination, the temperature-dependent Brosa model from Sec. II and the nuclear reaction code ALICE-91 as described in Sec. III enable the prediction of preneutron emission as well as postneutron emission mass yields in intermediate-energy light particle-induced fission reactions. After the determination in ALICE-91 of all contributions to the fission cross section by excited evaporation residues, which are characterized by $\sigma_F(A,Z,E^*)$, the temperature-dependent Brosa model computes for each configuration (A,Z,E^*) the corresponding fission-fragment mass yield curve. In the end, all these curves are summed with their proper weight given by $\sigma_F(A,Z,E^*)$.

Figure 37 illustrates the coupling between the temperature-dependent Brosa model and ALICE-91. Part of the contents from Sec. II is grouped in a dashed box situated in the upper right corner of the figure. These fission-mode calculations are performed only once to construct files containing the fission barrier parameters and prescission shapes of the investigated nuclides as indicated in Fig. 8. This information serves as input for the on-line mass distribution calculations.

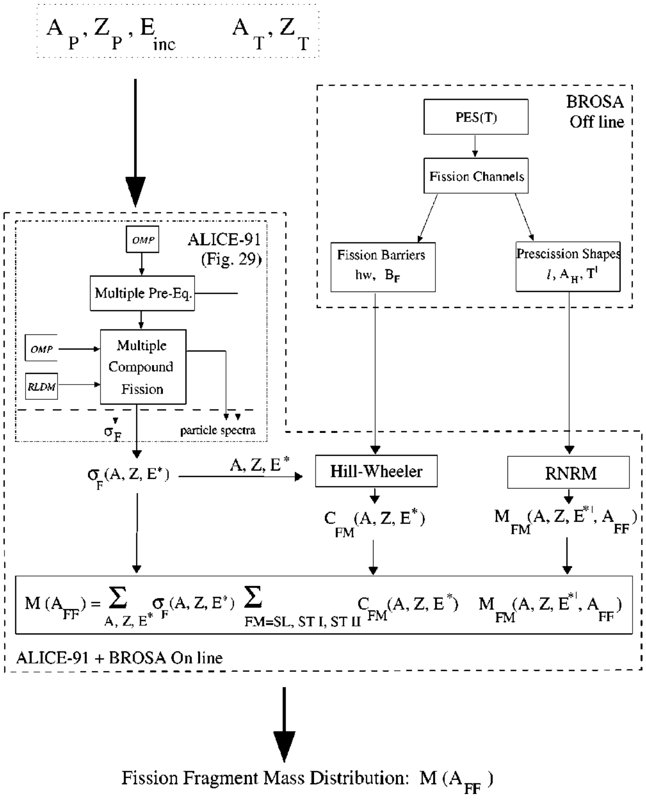

FIG. 37. Schematic overview illustrating the coupling of ALICE-91 and the temperature-dependent Brosa model. The subscript FM denotes the three dominant fission modes SL, ST I, and ST II. M_{FM} is the mass yield curve of a specific fission mode and C_{FM} its relative contribution.

Projectile, incoming energy, and target specifications form the main input (dotted box in top left corner) of these on-line calculations together with the ALICE-91 level density input parameters: a_n and a_f/a_n, the role of which has been already highlighted in the previous section. The calculation starts with an ALICE-91 run, which is indicated in the picture by a simplified version of Fig. 29 inside the dot-dashed frame. In this run, ALICE-91 keeps track of the flux going into fission for each individual isotope per excitation energy bin encountered in the Weisskopf-Ewing evaporation stage. Besides the normal output of the particle spectra and the total fission cross section, the fission cross section per fissioning isotope and excitation energy bin $\sigma_F(A,Z,E^*)$ is listed at the end.

For each configuration (A,Z,E^*) the program, subsequently, calls a subroutine of which the task is twofold. First of all the relative contributions $C_{FM}(A,Z,E^*)$ of the three predominant fission modes SL, ST I, and ST II are determined according to the recipe provided in Sec. II E. This happens inside the box, which carries the label Hill-Wheeler and uses the fission barrier parameters as input. The second task comprises the calculation of the mass yield curve $M_{FM}(A,Z,E^{*\prime},A_{FF})$ with the help of the RNRM based on the fission mode, the configuration $(A,Z,E^{*\prime})$ and the prescission shape parameters. Here, the loss and gain of excitation energy in crossing the barrier is taken into account

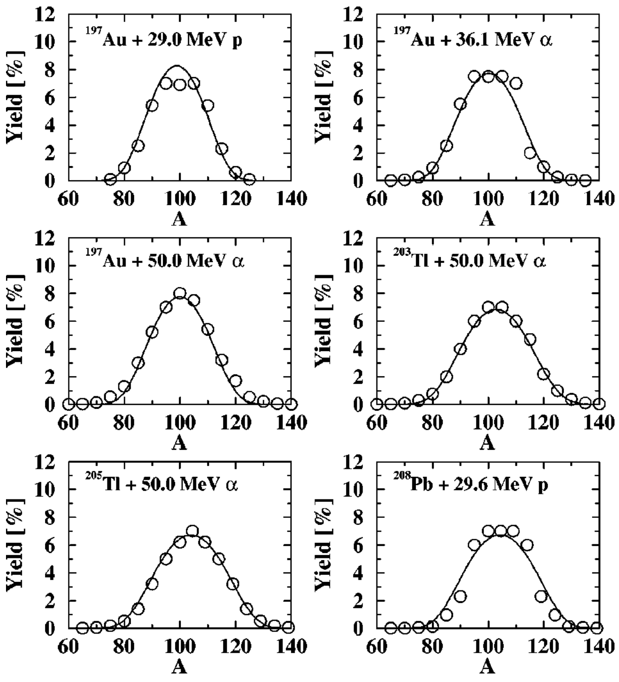

FIG. 38. Normalized preneutron emission mass yields for the reactions specified in each graph. The experimental data are taken from Refs. [59,60]. The lines correspond to the calculations.

into a new excitation energy $E^{*\prime}$ at scission. This is the procedure from Sec. II G. The computed preneutron emission mass distribution is, subsequently, corrected for the postscission neutron multiplicities (Sec. II G 2). In this manner, the postneutron emission mass yields are constructed. The final fission *fragment* mass distribution $M(A_{FF})$ is simply obtained by adding all separate preneutron emission mass yields $M_{FM}(A,Z,E^{*\prime},A_{FF})$ with the relative contributions $C_{FM}(A,Z,E^{*})$ and the fission cross sections $\sigma_F(A,Z,E^{*})$ as weights. Obviously, a completely equivalent approach gives rise to the final fission *product* mass distribution $M(A_{FP})$.

In the next sections predicted mass yields are compared to experimental data for subactinide and actinide fission between 15 and 200 MeV. Moreover, an investigation is included regarding the transition between asymmetric and symmetric fission in going from the line of stability towards neutron-deficient nuclides in the actinide region.

B. Mass yields in subactinide fission

The results from the ALICE-91 plus temperature-dependent Brosa model calculations for light particle-induced fission reactions in subactinide targets are shown in Figs. 38 and 39. In the case of subactinide targets it is not possible to calculate the competition between symmetric and asymmetric fission modes. In Sec. II, results of the fission channel search in ^{208}Pb exhibit rather broad and strangely shaped outer barriers, which makes a fit of these barriers with a parabola impossible. Hence the Hill-Wheeler approach cannot be applied. In all calculations in this section the asymmetric fission modes are discarded. Only the symmetric superlong mode is taken into account for subactinides.

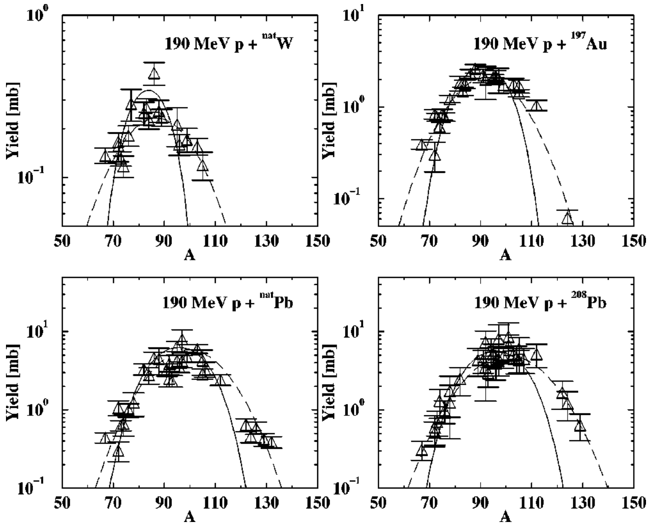

FIG. 39. Postneutron emission mass yields in proton-induced fission of ^{nat}W, ^{197}Au, ^{nat}Pb, and ^{208}Pb at 190 MeV obtained from Ref. [61]. The triangles denote the experimental data. The dashed line originates from the fit of a single Gaussian made by the authors and the solid line belongs to the calculation.

The experimental data included in Fig. 38 are taken from the extensive work on subactinide fission by Itkis *et al.* [59,60]. Examples of proton and alpha-induced fission between 29 and 50 MeV are given. In general, the agreement with the calculations is very good both for the position of the most probable mass and the width of the distribution. In the case of the 29-MeV proton-induced reactions, the calculations deviate at most 15% from the experimental values, but on average the agreement is much better. The assumption that for these nuclides asymmetric fission can be neglected seems valid for these energies.

The yields are normalized. Therefore also the uncertainty in the prediction of the overall fission cross section has to be incorporated. The calculations are performed with the level density parameters from Sec. III C. These values stem from a fit to the experimental neutron and proton-induced fission cross sections for ^{209}Bi and ^{197}Au. The basic assumption made is that the saddle-point to ground-state ratios a_f/a_n vary smoothly over the isotopes and hence that the ratios for ^{208}Pb and ^{203,205}Tl lie in between those of ^{209}Bi and ^{197}Au. The fission cross sections in this region of the chart of nuclides can be predicted with an accuracy of 10%. This has to be added to the uncertainty in the prediction of the normalized yields.

The predictions in Fig. 39 for the production cross sections of fission-product masses in 190-MeV proton-induced fission of ^{nat}W, ^{197}Au, ^{nat}Pb, and ^{208}Pb are less satisfactory. The experimental data have been obtained from Ref. [61]. Figure 39 contains, apart from the experimental data and the calculation (solid line), also a Gaussian (dashed line) that originates from a fit to the data and is given by the authors. The calculation does a fairly good job in the description of the left wings and of the top, but in right wings the experimental yields are underestimated by one order of magnitude. The huge discrepancy for heavier masses is mainly the result of a too small predicted width. In addition, the predicted

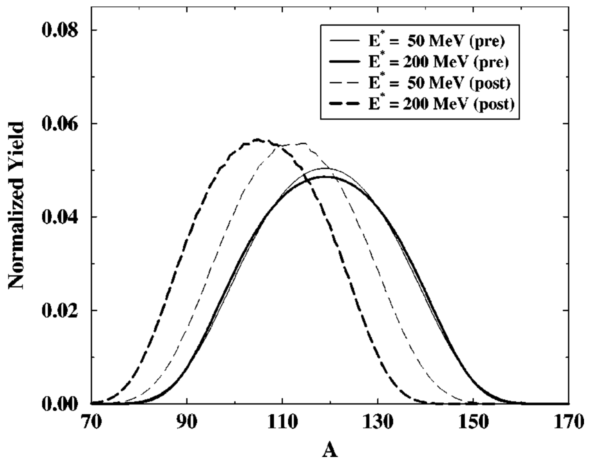

FIG. 40. Preneutron emission and postneutron emission mass yield curves for the superlong mode in a ^{238}U nucleus with an excitation energy at scission of 50 and of 200 MeV.

mean mass is shifted to lighter masses compared to the measured value. A lighter mean mass is related to an overestimation of the total number of evaporated mass units. This may indicate an underprediction of the energy carried away by the emitted particles prior to or after scission. A possible explanation of the first effect lies in the calculation of the postscission neutron multiplicities. With the temperature-dependent Brosa model as described in Sec. II the neutron evaporation between the saddle and scission points is neglected. This results in an excitation energy of the fragments which is too high. Since the division of the excitation energy available at scission between the two fragments goes proportional to the fragment mass, the heavy fragment will have a relatively higher postscission neutron multiplicity. Therefore it will shift more towards lower masses than the light fragment, thereby reducing the width of the mass distribution. A similar situation of a higher scission temperature occurs if the energy carried away by the prescission neutrons is too small. An overestimation of the postscission neutron multiplicity can also be caused by an underprediction of the energy required for the emission of neutrons by the fragments. The last two assumptions would simultaneously explain the smaller predicted mean mass, as already mentioned above.

A higher excitation energy at scission is linked to a higher scission temperature, and this also influences the width. The prescission shape half length is smaller at higher temperatures (see Fig. 24). A more compact shape results in a narrower mass distribution. On the other hand, an increase of the temperature in Eq. (62) enlarges the width. A comparison of the two effects shows that the latter is stronger. Figure 40 contains the preneutron emission and postneutron emission mass yield curves of the superlong mode for a ^{238}U nucleus with an excitation energy of 50 and 200 MeV at scission. The preneutron emission yield curve at 200 MeV is broader than the preneutron emission yield curve at 50 MeV, although the prescission shape is shorter around 200 MeV. The postneutron emission yield distribution at 200 MeV becomes narrower than the one around 50 MeV. This observation supports the explanation given above that the inclusion of postscission neutron emission in its present form reduces the width of the mass distribution. Whether the overprediction of the postscission neutron multiplicity is connected to an overestimation of the temperature at scission or to an underestimation of the energy required for the emission of a neutron by the fragments cannot be concluded from these data. The next section will shed some more light on this question.

TABLE III. Proton-induced subactinide fission cross sections obtained from experiment [61] and from ALICE-91 calculations. For comparison also the values stemming from the data compilation by Eismont *et al.* [58] are included.

	$^{\mathrm{nat}}$W	^{197}Au	$^{\mathrm{nat}}$Pb	^{208}Pb
σ_f^{Exp} (mb)	4.5±.5	32.8±3.3	94±9	88±8
$\sigma_f^{ALICE-91}$ (mb)	3.7	31.2	83.6	76.4
$\sigma_f^{Eismont}$ (mb)	3.7		88	74

Table III shows the fission cross sections resulting from experiment [61], the calculations, and the Eismont *et al.* [58] data compilations. ALICE-91 tends to underestimate the fission cross section with 10–15%.

C. Mass yields in actinide fission

In the case of actinide fission the full competition between the symmetric and asymmetric fission modes is taken into account. With these modes it becomes possible to describe a variety of shapes, which is needed to cover the whole range of intermediate energy fission between several MeV and 200 MeV. Preneutron emission mass yields in neutron-induced fission of ^{238}U for various different projectile energies are plotted in Fig. 41. The experimental data come from the work by Zöller *et al.* [62]. At an average incident neutron energy of approximately 13 MeV the mass distribution exhibits a pronounced asymmetric behavior. This asymmetric character persists up to an average neutron incident energy of roughly 100 MeV. Above this energy a broad mass yield curve remains, which still betrays some asymmetric components by its broad and flat top. What happens is that with increasing excitation energy the symmetric valley from low-energy fission fills up due to a stronger symmetric (SL) contribution. This forms the main contribution. Another much smaller effect is the widening of the asymmetric contributions.

The calculations of Fig. 41 show that almost everywhere the agreement is within 10% or even better. Figure 42 contains the same data and calculational results but on a logarithmic scale. This is done to enable a better comparison of the experimental data and the calculations in the tails of the distributions. At very high energies (around 200 MeV), the predictions and data start to deviate at extremely asymmetric yields by one order of magnitude. This is a similar effect as in the subactinide postneutron emission yields at 190 MeV of the previous section, but it is less strong. A possible explanation is that the predicted prescission shapes are too compact. The fact that the mean mass, the width, and the relative asymmetric and symmetric contributions come so close to the results found experimentally indicates that neither the calculated temperature at scission can be much too high nor

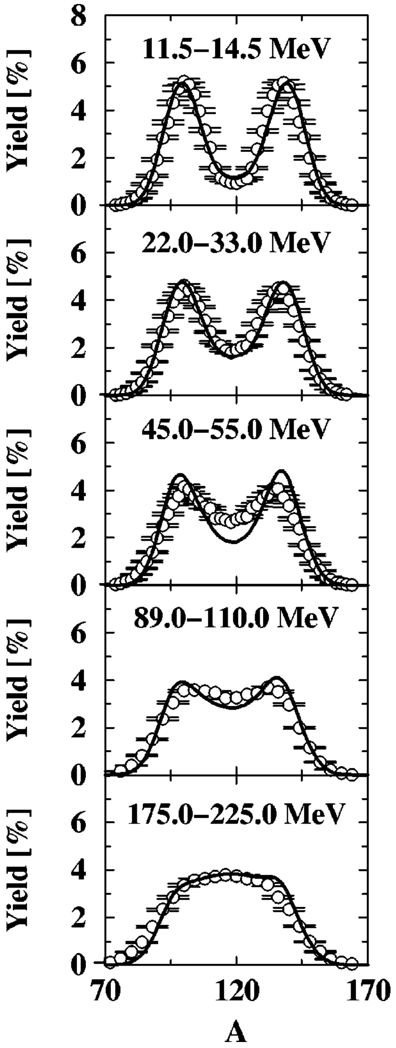

FIG. 41. Preneutron emission mass yields in neutron-induced fission reactions on ^{238}U with the neutron incoming energy range specified in the graphs. The saddle-point to ground-state level density ratios are fitted to reproduce the shape of the mass yield curve. Data are taken from Ref. [62].

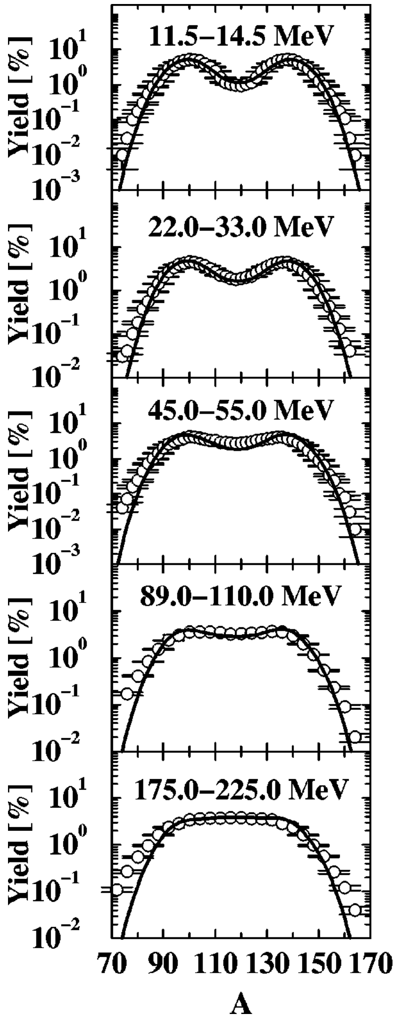

FIG. 42. Same as Fig. 41 but on a logarithmic scale. Data are taken from Ref. [62].

the calculated prescission neutron multiplicity can be much too low. This observation agrees with the supposition that the calculated postscission neutron multiplicity may be too high due to a wrong estimation of the energy required for the emission of neutrons by the fragments and not due to a scission temperature that is too high.

The predictions for these normalized yields are obtained by adjusting the saddle-point to ground-state level density ratios to reproduce the experimental mass yields. In Sec. III the influence on the prediction of the total fission cross section has already been examined. It turns out that the fission cross section in the reactions under study is overestimated by approximately 15%. The influence of this level density ratio is rather profound as can be concluded from Fig. 43. This figure shows the results of the mass yield calculations based on the level density ratios which perfectly describe the fission cross section (see Sec. III C). These ratios are lower than the ones used in Fig. 41. For low energies the difference is rather small (up to 30 MeV), but at higher energies the asymmetric contributions are overestimated. This is understandable, since fission is preceded by more evaporation and takes place at lower excitation energies with a smaller value of the ratio. The discrepancies with the experimental mass yield curves amount to 30%.

Figure 44 is included to illustrate the effect of taking a different prescission shape in the calculation. According to Brosa, the neck becomes unstable against rupture at the Rayleigh criterion. The results in Fig. 44 are obtained by assuming that scission already takes place at the Rayleigh criterion. This corresponds to more compact prescission shapes and hence to shorter necks. The consequence is obvious: the neck can break at less locations with equal probability. This causes the peaks to be narrower and the widths of the distributions are completely off.

Besides neutron-induced reactions, also proton-induced fission is investigated. In Fig. 45 the results are plotted for preneutron emission mass yields in proton-induced fission of ^{232}Th at three different energies. The experimental data are taken from Ref. [63]. For 13 and 20 MeV the agreement is again quite good (within 10%). The reaction at an incident energy of 53 MeV shows a wrong relative contribution of

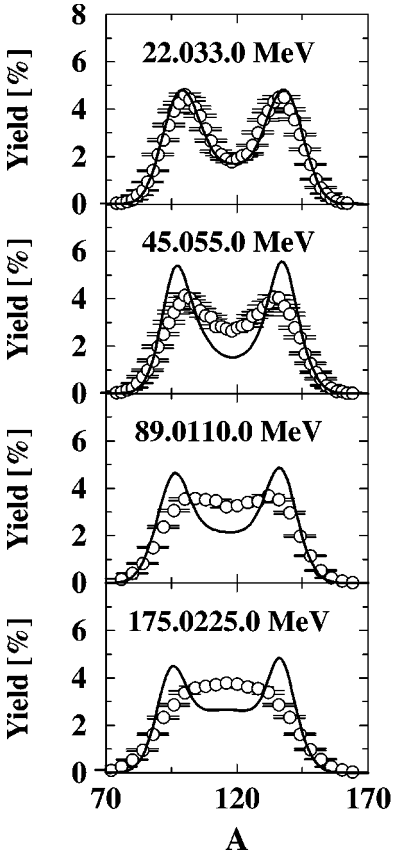

FIG. 43. Preneutron emission mass yields in neutron-induced fission reactions on ^{238}U. The saddle-point to ground-state level density ratios are fitted to reproduce the total fission cross section. Data are taken from Ref. [62].

asymmetric and symmetric fission. As will be further explained in the last section, thorium lies on the edge of the actinide region and is subject to a transition to symmetric fission which occurs much earlier than in the case of uranium. Apparently, the ALICE-91 plus temperature-dependent Brosa model is not able to predict this transition accurately. Up to 50 MeV, the prediction of the fission cross section ends up within 10% of the experimental values.

Figure 46 shows preneutron emission mass yields in proton-induced fission of ^{226}Ra and ^{238}U [64,65]. In the case of 13-MeV protons on ^{226}Ra the prediction gives a triple-humped distribution in accordance with experimental observations. Unfortunately, the relative contributions of the fission modes are incorrect. Furthermore, the position of the asymmetric peak does not agree with the experimental data. This is due to the fact that the ST I mode is predominant in the calculation, while from the experimental data the peak around mass 140 indicates a strong contribution of the ST II mode. The first problem resembles the underprediction of symmetric fission in 53-MeV proton-induced reactions in ^{232}Th as mentioned in the previous paragraph. The outcome of the calculations for ^{238}U at 20 and 60 MeV incident energies is acceptable. On top of the 10% uncertainty in the normalized mass yields, an additional uncertainty of 15% in the total fission cross section enters.

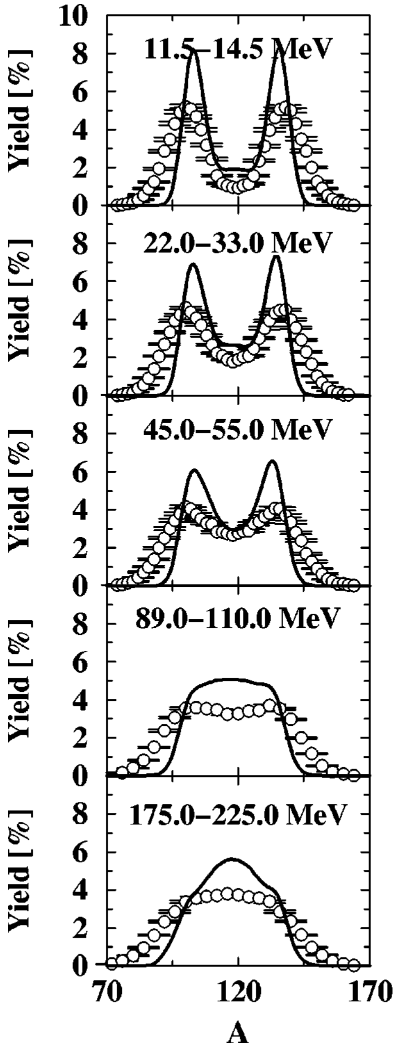

FIG. 44. Preneutron emission mass yields in neutron-induced fission reactions on ^{238}U with the prescission shapes taken at the Rayleigh criterion. Data are taken from Ref. [62].

Postneutron emission mass yields can be found in Figs. 47 and 48. Figure 47 displays postneutron emission mass yields in neutron-induced fission of ^{238}U [62]. The same incident energy ranges are chosen as for the preneutron emission yields. The agreement for the 13- and 28-MeV incident energies is excellent. At higher energies the effect from the excessive postscission neutron evaporation is present. The underprediction of the width of the preneutron emission mass yield curve is enhanced by the postscission neutron evaporation. This has already been encountered and explained in the previous section and further elucidated in the beginning of this section. The heavy fragments lose too many neutrons, which leads to an underprediction in the right wing of the distribution and to an overprediction on the left-hand side. Especially the mass yield curve around 200 MeV suffers from this effect to the same extent as the subactinides in proton-induced reactions at 190 MeV (Fig. 39).

Unfortunately, the experimental data for other nuclides are limited to neutron energies around 14 MeV. Figure 48 includes data for four different nuclides: ^{232}Th, ^{233}U, ^{242}Pu,

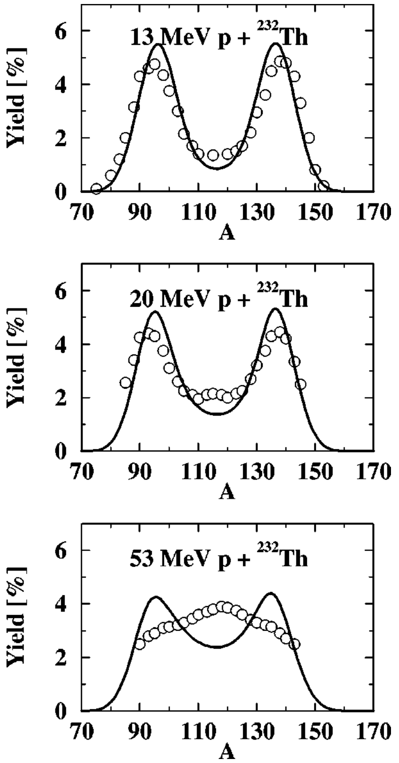

FIG. 45. Preneutron emission mass yields in proton-induced fission reactions on ^{232}Th for the incoming energies given in the graphs. Data are taken from Ref. [63].

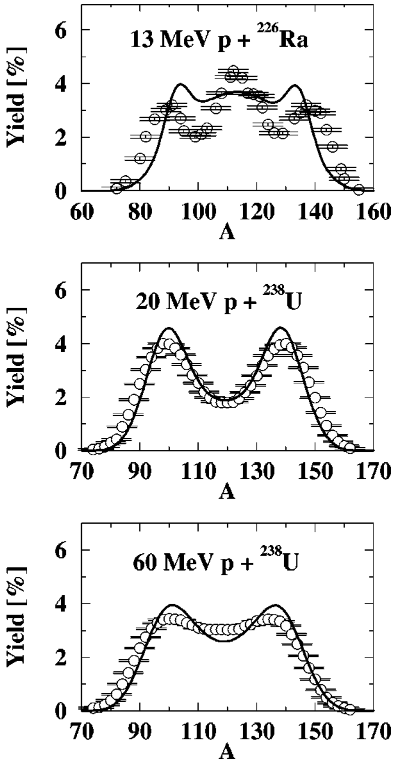

FIG. 46. Preneutron emission mass yields in proton-induced fission reactions on ^{226}Ra and ^{238}U for the incident energies given in the graphs. Data are taken from Refs. [64,65].

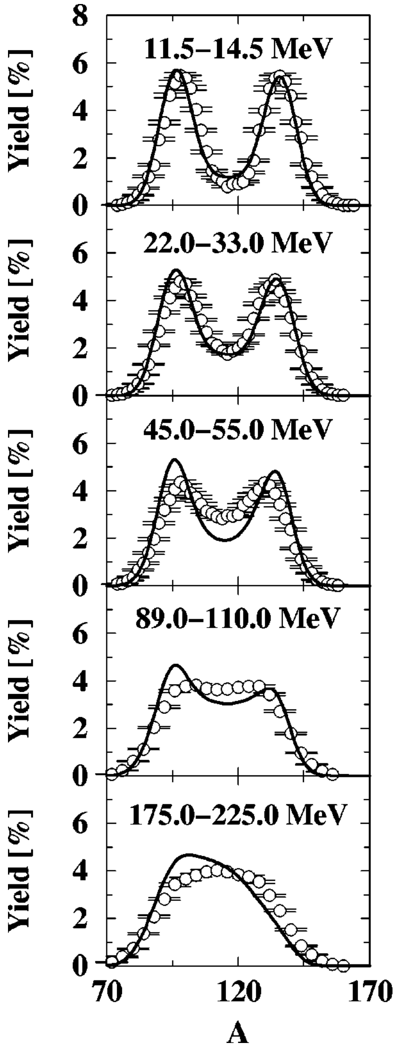

FIG. 47. Postneutron emission mass yields in neutron-induced fission reactions on ^{238}U. The neutron incident energy ranges are denoted in the graphs. Data are taken from Ref. [62].

and ^{241}Am [66–69]. At the corresponding excitation energies the postscission neutron evaporation does not yet spoil the outcomes. The prediction in the wings of the mass distributions deviates from experiment with maximally 30% for ^{232}Th, ^{242}Pu, and ^{241}Am. However, in the case of ^{233}U the right tail is underpredicted by a factor of 10. On the top of the distribution and in the symmetric valley the agreement is within 20%, except in some mass regions of ^{232}Th where the calculated yields lack the small symmetric hump.

D. Transition from symmetric to asymmetric fission

From all mass yield curves seen so far in the previous two sections, it can be concluded that somewhere at the edge of the actinide region a transition takes place between symmetric and mixed (symmetric plus asymmetric) fission. Moreover, observations by Schmidt *et al.* [11] suggest a change towards symmetric fission in the neutron-deficient part of the actinide region. In addition, an increase in symmetric fission is observed with increasing excitation energy. The question arises whether this last effect is mainly due to the vanishing

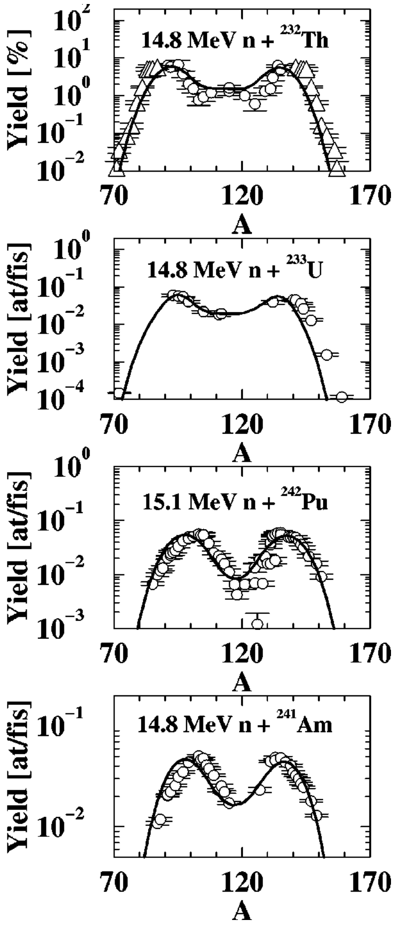

FIG. 48. Postneutron emission mass yields in neutron-induced fission reactions as specified in the graphs. Data are taken from Refs. [66–69]. The triangles in the upper graph correspond to data read from a table, whereas the circles are read from a figure.

of asymmetric fission modes with increasing excitation energy or to the contributions of more and more neutron-poor isotopes with an intrinsic symmetric behavior.

Figure 49 shows mass distributions of various isotopes between actinium and uranium labeled by the element name and neutron number. The calculations are carried out for nuclides with an excitation energy of 10 MeV. The gradual change from asymmetric and mixed to symmetric fission is clearly visible. Near the valley of stability, at the right-hand side of the plot, fissioning isotopes tend to produce mass distributions with a strong asymmetric signature. At the left-hand side the resulting mass yields are entirely symmetric or possess at least a large symmetric share. A solid line connects the isotopes for which the symmetric hump exceeds the asymmetric humps for the first time in going towards neutron-poor nuclides starting from stability. This is taken as a crude measure for the transition. The dot-dashed line represents a condition by Chung and Hogan [70,71] which also marks the transition from symmetric to asymmetric (mixed) fissioning isotopes. The dashed line corresponds to a calculation by Möller [72] who determined the stability of the saddle-point configuration against asymmetric deformations. The lines belonging to Chung and Hogan and Möller have in common that they run more or less parallel to the line of stability. The line originating from the ALICE-91 plus temperature-dependent Brosa model calculations, however, is perpendicular to these lines. This completely different behavior is also observed by Schmidt *et al.* [11] in the charge distributions of the same fissioning isotopes at excitation energies peaked around 11 MeV. Here the transition marked by the dotted line also tends to occur along a line perpendicular to the Möller line. The prediction by the ALICE-91 plus temperature-dependent Brosa model exhibit therefore the same tendency as experimentally observed. In conclusion, at low energies the transition seems to take place at less neutron-poor nuclides for thorium and actinium than for uranium.

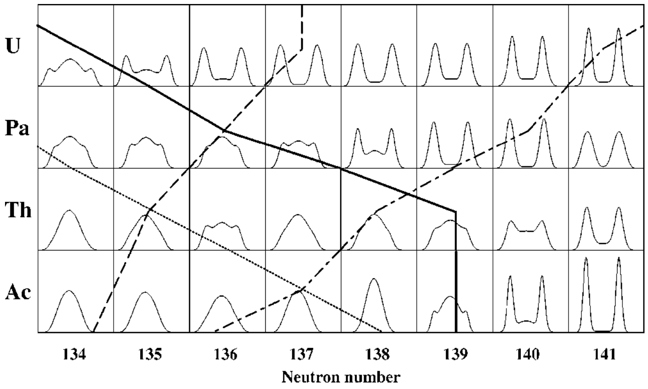

FIG. 49. Mass distributions of various isotopes labeled by the element name and neutron number. The calculations are performed at a fixed excitation energy of 10 MeV. The thick solid line connects isotopes for which the symmetric hump exceeds the asymmetric humps for the first time starting from stability and going towards neutron-poor nuclides. The dotted line is obtained in an equivalent manner from charge distributions measured by Schmidt *et al.* [11]. The dot-dashed line represents the condition by Chung and Hogan [70,71] and the dashed line corresponds to a calculation by Möller [72].

The portion symmetric and asymmetric fission depends on the excitation energy. Therefore similar calculations are carried out for an excitation energy of 20 MeV (Fig. 50). Because the excitation energy lies well above the barriers, all fission modes present have a reasonable contribution. This explains the mixed mass yields visible in all graphs. Appar-

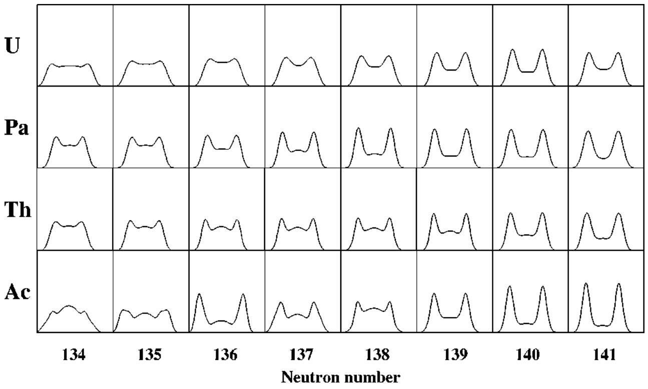

FIG. 50. Same as Fig. 49 but for an excitation energy of 20 MeV.

ently, only at considerably low energies, symmetric fission is preferred by the neutron-deficient isotopes as well as by most actinium isotopes at the edge of the actinide region. Since the melting of fission modes happens in beta-stable and very neutron-deficient nuclides at a comparable rate (see, e.g., Sec. II F), the situation of Fig. 50 persists up to a certain excitation energy, above which an overall and gradual transition to symmetry occurs simultaneously for all isotopes. Hence in the calculations presented here the increase of symmetric fission at high energies is fed more by the disappearance of the asymmetric fission modes due to the vanishing of shell effects and less by a larger contribution of neutron-deficient nuclides due to the preceding neutron evaporation.

In the previous section a systematic underprediction of the symmetric component in the description of intermediate-energy fission of thorium and radium has been observed. Two effects may be responsible for this. The increase of the symmetric component in these elements may be too slow with excitation energy or, equivalently, the asymmetric fission modes do not vanish in time. The alternative possibility is a lack of symmetric fission in neutron-poor nuclides due to wrong barrier parameters resulting in an overestimation of asymmetric fission at higher energies, or due to an overprediction of the excitation energy in these nuclides. Based on the comparisons between calculations and experimental results shown here it is not possible to draw a final conclusion. Perhaps that the future will bring other experimental data that will help to solve the question on how the transition between symmetric and asymmetric fission takes place.

V. SUMMARY AND OUTLOOK

A. Summary

In intermediate-energy fission studies the keyword is multichance fission. The evolution of an entirely equilibrated nucleus from its ground-state shape to the scission point is thought to proceed at a pace comparable to the emission of light particles. The process of sequential particle evaporation populates many intermediate nuclides characterized by (A_{CN},Z_{CN},E^*_{CN}). Each nuclide in each excitation energy bin makes a decision: to fission or to evaporate further. Hence in the description of fission two main ingredients can be distinguished: a model to determine the fission cross sections for all fissioning systems as a function of their excitation energies $\sigma_F(A_{CN},Z_{CN},E^*_{CN})$ and a model to predict the fission-fragment and fission-product yields for each set of (A_{CN},Z_{CN},E^*_{CN}).

The original Brosa model [12] has been extended in various ways. First of all, the temperature is added to the calculation of the potential energy landscape of the nucleus. In this manner, the incorporated melting of the shell effects naturally gives rise to the vanishing of asymmetric fission modes ST I and ST II with increasing excitation energies. Second, the relative contributions of the different fission modes are evaluated with the Hill-Wheeler penetrability through inverted parabolic barriers using ground-state level densities and temperature-dependent barrier parameters. The classic random neck-rupture model, subsequently, translates the rupture probability as a function of the position at the neck of the scissioning nucleus into the preneutron and postneutron emission mass yield curve. Linking this result with the fission cross section contributions by all possible fissioning systems (A_{CN},Z_{CN},E^*_{CN}) as computed by ALICE-91 [38], the total preneutron emission and postneutron emission mass yields may be determined for any imaginable light particle-induced fission reaction from 15 up to roughly 200 MeV. In this way, the competition with all other outgoing channels is automatically taken into account. By separating the calculation of the fission cross section from the fission fragment properties, the final uncertainty in the prediction is a superposition of the uncertainties stemming from both steps.

TABLE IV. Accuracies obtained from comparing the predictions with experimental data for incident energies between 15 and 200 MeV and isotopes as treated in Sec. IV. The relative uncertainties in the proton and neutron-induced fission cross sections as well as in the preneutron and postneutron emission mass yields are given.

	Subactinide region	Actinide region		
	$Z<84$	$Z<91$	Uranium	$Z>93$
$\sigma_F(p,f)$	10–100 %	10–20 %	10%	
$\sigma_F(n,f)$	10–15 %	10–20 %	10–15 %	20%
$Y_{pre}(A)$	10–15 %	10–50 %	10%	
$Y_{post}(A)$	50–1000 %		10–1000 %	30%

Actinide nuclides turn out to have three dominant fission modes: the symmetric superlong mode (SL), and the asymmetric modes standard I (ST I), and standard II (ST II), whereas subactinides possess only one asymmetric mode ST in addition to SL in the Brosa calculations. For subactinides, asymmetric fission is completely neglected in the present calculations. The outer barrier is not described well with a parabola, which disenables the determination of the relative fission mode weights by a Hill-Wheeler approach. The fission barrier heights resulting from the channel searches in the PES agree very well with experimental values for the inner barriers. The outer barriers, however, are much too high. From the final mass distributions it can be concluded, nevertheless, that these outer barriers suffice to determine correctly the relative weights of the fission modes in most cases.

Mass yields can be predicted with a proper choice of both the ground-state to saddle-point level density parameter ratio a_f/a_n and the prescission shapes. The prescission shapes are fixed by applying the same recipe to all nuclei. This leaves a_f/a_n as the only parameter which is tuned to reproduce at best both the fission cross section and the mass yield curve for a given reaction. The obtainable accuracy depends in general on the incident energy as well as on the isotope investigated. Table IV contains a summary of the uncertainties. They are extracted from comparing the predictions for the total fission cross sections as well as for the preneutron and postneutron emission mass yields with experimental data. The incident nucleon energies range from 15 to 200 MeV and the isotopes are either subactinides or actinides. In Table IV the actinide region is subdivided into (a) the nuclides on the edge marking the transition to low-energy symmetric fission, (b) uranium for which a large amount of data is available, and (c) the heavier actinides. The predictive power changes drastically with observable, nuclide, and excitation energy.

The prediction of the total fission cross section is fairly accurate. Only in the case of the subactinides, for which the probabilities become very small, deviations up to 100% can occur. The determination of preneutron emission mass yields is satisfactory. The good agreement for uranium at energies as high as 200 MeV suggests that the temperature-dependent LDM does not break down above a temperature of 2.0 MeV. This value has been given as the validity boundary as mentioned in Sec. II C. Only in fission of ^{226}Ra and ^{232}Th the model cannot correctly describe the experimentally observed transition to symmetric fission. Asymmetric fission persists up to too high incident energies. This leads to deviations between 10% at low energies and 50% at high energies in the fission-fragment mass yields. Whether this stems from too slowly vanishing asymmetric fission with increasing excitation energies or from a lack of symmetric fission contributions from neutron-deficient nuclides could not be concluded from the results in this work. In general, the calculated postneutron emission mass yields are too narrow: the light wing and the top are reproduced within 50% or better, whereas the heavy wing is underestimated by one order of magnitude. This is probably related to an overestimation of the postscission neutron multiplicity. The model neglects the neutron evaporation between the saddle point and the scission point. This leaves too much excitation energy in the fission fragments. Consequently, the heavier fragment, which receives a larger portion of the excitation energy of the fissioning system, evaporates absolutely more neutrons than the lighter fragment. This reduces the width of the final mass distribution. Since, however, the calculated mean mass of the preneutron emission mass yield curves agrees very well with the experimental values, the prescission neutron multiplicity, which momentarily excludes neutron evaporation between the saddle point and the scission point, cannot be completely wrong. Furthermore, the temperature of the fissioning system cannot be far too high, because of the correctly reproduced relative contributions of the different fission modes in the calculated preneutron emission mass yield distributions. Therefore a more likely explanation is provided by the supposition that the fragments evaporate too many neutrons because of an underestimation of the energy required for the emission of particles.

B. Outlook

Future developments in the theory may contribute to a better prediction of either the multichance fission process or the fission-fragment properties. Three major extensions possible in the calculation of the fission-fragment properties consist of including the charge distribution, the TKE, and the neutron emission between the saddle point and scission point. The addition of the TKE requires only a minor effort, since this is already computed by the RNRM. It only requires implementation into the coupling with ALICE-91. The calculation of the charge distribution does not follow from the RNRM. Here another model, possibly the scission point model by Wilkins *et al.* [6], has to be introduced. The neutron emission from saddle point to scission point may be taken into account in some effective way by assuming that part of the available excitation energy is transformed into neutrons emitted from the fissioning system before scission takes place.

Ingredients in the temperature-dependent Brosa model itself also might lead to further refinements. The parametrization of the deforming nucleus may require more than the five parameters which are presently used. The addition of some extra parameters will allow the nucleus more freedom in the choice of its shapes and hence in the fission channel. This may result in a better agreement between the experimentally determined outer barrier heights and the calculated values. Moreover, the fact that only the shell effects of the complete fissioning nucleus are computed can possibly account for deviations observed in the predicted average heavy fragment mass. The inclusion of shell effects in the fragments may turn out to be indispensable for an even more reliable prediction of this quantity. Another refinement may originate from the inclusion of the collective enhancement in the calculation of the transmission through the different outer barriers in order to determine the relative weights of the fission modes. For this purpose, a calculation of the moments of inertia at each of the saddle points will be necessary. In this work, the ground-state level density is used in combination with temperature-dependent barriers disregarding the change in collective effects between the ground state and the various outer saddles.

Improvements are also achievable in the description of the multichance fission process. This may be connected either to the replacement of the Bohr-Wheeler approach for a single-humped barrier, as used in ALICE-91, by a more sophisticated treatment, or to a better understanding of the other reaction channels which influence indirectly the fission outcomes through their competition with the fission process.

The research presented in this manuscript merely forms a step in the process of acquiring a deeper understanding of the fission process at intermediate energies. The combination of future refinements in the calculations and the appropriate additional experiments might in the end provide an answer to the still open question about the true nature of the observed energy and mass-dependent transition between asymmetric and symmetric fission.

ACKNOWLEDGMENTS

The authors wish to thank K.-H. Schmidt and S. Hilaire for many helpful discussions regarding the use of temperature-dependent fission barriers.

APPENDIX: WEIGHTS OF FISSION MODES

If the transmission of the first barrier is denoted by Tr_A and that of the second barrier by Tr_B, the total transmission coefficient is given by:

$$\mathrm{Tr}_F = \frac{\mathrm{Tr}_A\,\mathrm{Tr}_B}{\mathrm{Tr}_A + \mathrm{Tr}_B}. \qquad \text{(A1)}$$

This is the same as Eq. (58) in Sec. II. This expression is only valid if at least one of the barriers is lower than the excitation energy, and hence one of the single transmission coefficients is close to unity or greater. For all nuclides considered in this work, the theoretical inner barrier is always much lower than the theoretical outer barrier. Therefore Tr_{inner} is much larger than the transmission coefficients through the outer barriers. The separate total transmission coefficients of the three dominant fission modes SL, ST I, and ST II have the following form:

$$\mathrm{Tr}_{SL} = \frac{\mathrm{Tr}_{SL,outer}\,\mathrm{Tr}_{inner}}{\mathrm{Tr}_{SL,outer} + \mathrm{Tr}_{inner}}. \qquad \text{(A2)}$$

The weight W of the superlong mode becomes (expressions for the other fission modes are completely equivalent)

$$W_{SL} = \frac{\mathrm{Tr}_{SL}}{\mathrm{Tr}_{SL} + \mathrm{Tr}_{STI} + \mathrm{Tr}_{STII}} = \frac{1}{1 + \dfrac{\mathrm{Tr}_{STI,outer}}{\mathrm{Tr}_{SL,outer}}\,\dfrac{\mathrm{Tr}_{SL,outer} + \mathrm{Tr}_{inner}}{\mathrm{Tr}_{STI,outer} + \mathrm{Tr}_{inner}} + \dfrac{\mathrm{Tr}_{STII,outer}}{\mathrm{Tr}_{SL,outer}}\,\dfrac{\mathrm{Tr}_{SL,outer} + \mathrm{Tr}_{inner}}{\mathrm{Tr}_{STII,outer} + \mathrm{Tr}_{inner}}}, \qquad \text{(A3)}$$

which may be approximated as follows:

$$W_{SL} \approx \frac{\mathrm{Tr}_{SL,outer}}{\mathrm{Tr}_{SL,outer} + \mathrm{Tr}_{STI,outer} + \mathrm{Tr}_{STII,outer}}. \qquad \text{(A4)}$$

This last step is valid if $\mathrm{Tr}_{inner} \gg \mathrm{Tr}_{SL,outer}$, $\mathrm{Tr}_{inner} \gg \mathrm{Tr}_{STI,outer}$, and $\mathrm{Tr}_{inner} \gg \mathrm{Tr}_{STII,outer}$, i.e.,

$$\frac{\mathrm{Tr}_{SL,outer} + \mathrm{Tr}_{inner}}{\mathrm{Tr}_{STI,outer} + \mathrm{Tr}_{inner}} \approx 1. \qquad \text{(A5)}$$

Another way to arrive at the same result for the weight of the fission modes is to neglect the first barrier completely from the beginning.

---

[1] http://www.sckcen.be/research/reactorsafety/fuel/myrrha/myrrha_home.html

[2] A. J. Koning (private communication).

[3] V. P. Eismont, A. V. Prokofyev, A. N. Smirnov, K. Elmgren, J. Blomgren, H. Condé, J. Nilsson, N. Olsson, T. Rönnqvist, and E. Tranéus, Phys. Rev. C **53**, 2911 (1996).

[4] V. P. Eismont, A. V. Prokofyev, I. V. Ryzhov, A. N. Smirnov, G. A. Tutin, H. Condé, K. Elmgren, and N. Olsson, *Third International Conference on Accelerator Driven Transmutation Technologies and Applications*, edited by H. Condé, Prague, Czech Republic, 1999.

[5] A. Yu. Donets, A. V. Evdokimov, A. V. Fomichev, T. Fukahori, A. B. Laptev, G. A. Petrov, O. A. Shcherbakov, Yu. V. Tuboltsev, and A. S. Vorobyev, JINR Report E3-98-212, Dubna, Russia, 1999, p. 357.

[6] B. D. Wilkins, E. P. Steinberg, and R. R. Chasman, Phys. Rev. C **14**, 1832 (1976).

[7] H. J. Specht, Phys. Scr. **10A**, 21 (1974).

[8] G. A. Kudyaev, Yu. B. Ostapenko, and G. N. Smirenkin, Yad. Fiz. **45**, 1534 (1987) [Sov. J. Nucl. Phys. **45**, 951 (1987)].

[9] G. A. Kudyaev, Yu. B. Ostapenko, E. M. Rastopchin, and G. N. Smirenkin, Yad. Fiz. **47**, 1540 (1988) [Sov. J. Nucl. Phys. **47**, 976 (1988)].

[10] J. Benlliure, A. Grewe, M. de Jong, K.-H. Schmidt, and S. Zhdanov, Nucl. Phys. **A628**, 458 (1998).

[11] K.-H. Schmidt, S. Steinhäuser, C. Böckstiegel, A. Grewe, A. Heinz, A. R. Junghans, J. Benlliure, M. de Jong, J. Müller, M. Pfützner, and B. Voss, Nucl. Phys. **A665**, 221 (2000).

[12] U. Brosa, S. Großmann, and A. Müller, Phys. Rep. **197**, 167 (1990).

[13] K.-H. Schmidt, A. Heinz, H.-G. Clerc, B. Blank, T. Brohm, S. Czajkowski, C. Donzaud, H. Geissel, E. Hanelt, H. Irnich, M. C. Itkis, M. de Jong, A. Junghans, A. Magel, G. Münzenberg, F. Nickel, M. Pfützner, A. Piechaczek, C. Röhl, C. Scheidenberger, W. Schwab, S. Steinhäuser, K. Sümmerer, W. Trinder, B. Voss, and S. V. Zhdanov, Phys. Lett. B **325**, 313 (1994).

[14] V. A. Rubchenya, J. Äystö, P. Dendooven, S. Hankonen, A. Jokinen, W. H. Trzaska, D. N. Vakhtin, J. C. Wang, A. V. Evsenin, S. V. Khlebnikov, A. V. Kuznetsov, V. G. Lyapin, O. I. Osetrov, G. P. Tiourin A. A. Alexsandrov, and Yu. E. Penionzhkevich, in *Nuclear Fission and Fission-product Spectroscopy: 2nd International Workshop*, Seyssins, France, edited by G. Fioni, H. Faust, S. Oberstedt, and F.-J. Hambsch, AIP Conf. Proc. No. 447 (AIP, Woodbury, NY, 1998), p. 453.

[15] F. Atchison, in ‘‘Targets for Neutron Beam Spallation Sources,’’ Report No. Jül-Conf-34, Kernforschungsanlage Jülich GmbH, Germany, 1980.

[16] U. Brosa and S. Grossman, Phys. Lett. **126B**, 425 (1983); Z. Phys. A **310**, 177 (1983); J. Phys. G **10**, 933 (1984); U. Brosa, Phys. Rev. C **32**, 1438 (1985).

[17] A. Turkevich and J. B. Niday, Phys. Rep. **84**, 52 (1951).

[18] V. V. Pashkevich, Nucl. Phys. **A169**, 275 (1971).

[19] V. M. Strutinsky, Yad. Fiz. **3**, 614 (1966) [Sov. J. Nucl. Phys. **3**, 449 (1966)].

[20] J. N. P. Lawrence, Phys. Rev. **139**, 1227 (1965).

[21] P. Möller and A. Iwamoto, Phys. Rev. C **61**, 047602 (2000).

[22] V. A. Chepurnov, Yad. Fiz. **5**, 955 (1968) [Sov. J. Nucl. Phys. **6**, 696 (1968)].
[23] M. Sano and S. Yamasaki, Prog. Theor. Phys. **29**, 397 (1963).
[24] P. Decowski, W. Grochulski, M. Marcinkowski, K. Siwek, and Z. Wilhelmi, Nucl. Phys. **A110**, 129 (1968).
[25] L. G. Moretto, Nucl. Phys. **A185**, 145 (1972).
[26] M. Diebel, K. Albrecht, and R. W. Hasse, Nucl. Phys. **A355**, 66 (1981).
[27] N. H. Allal and M. Fellah, Phys. Rev. C **48**, 1656 (1993).
[28] W. D. Myers and W. J. Swiatecki, Nucl. Phys. **81**, 1 (1966).
[29] W. D. Myers and W. J. Swiatecki, Ark. Fys. **36**, 343 (1967).
[30] R. W. Hasse and W. Stocker, Phys. Lett. **44B**, 26 (1973).
[31] A. Stocker, Phys. Lett. **46B**, 59 (1973).
[32] H. J. Krappe, J. R. Nix, and A. J. Sierk, Phys. Rev. C **20**, 992 (1979).
[33] A. J. Sierk, Phys. Rev. C **33**, 2039 (1986).
[34] R. Vandenbosch and J. R. Huizenga, *Nuclear Fission* (Academic, New York, 1973).
[35] W. D. Myers and W. J. Swiatecki, Nucl. Phys. **A612**, 249 (1997).
[36] J. W. Rayleigh, Proc. London Math. Soc. **10**, 4 (1878).
[37] P. Siegler, F.-J. Hambsch, S. Oberstedt, and J. P. Theobald, Nucl. Phys. **A594**, 45 (1995).
[38] M. Blann, presented at the *Workshop on Computation and Analysis of Nuclear Data Relevant to Nuclear Energy and Safety*, Trieste, Italy, 1992. M. Blann, LLNL Report No. UCRL-JC-109052 (1991).
[39] S. Bjǿrnholm and J. E. Lynn, Rev. Mod. Phys. **52**, 725 (1980).
[40] Handbook for Calculations of Nuclear Reaction data: Reference input parameter library, IAEA-TECDOC-1034, 1998.
[41] C. Wagemans, *The Nuclear Fission Process* (CRC Press, Boca Raton, 1991).
[42] D. L. Hill and J. A. Wheeler, Phys. Rev. **89**, 1102 (1953).
[43] A. Gilbert and A. G. W. Cameron, Can. J. Phys. **43**, 1446 (1965).
[44] A. V. Ignatyuk, G. N. Smirenkin, and A. S. Tishin, Yad. Fiz. **21**, 485 (1975) [Sov. J. Nucl. Phys. **21**, 255 (1975)].
[45] N. P. D'Jacnenko, B. D. Kuz'minov, V. F. Mitrofanov, and A. I. Sergachjov, *Fourth All Union Conference on Neutron Physics*, Vol. 3, Kiev, USSR, 1977, p. 171.
[46] J. Blachot, NEANDC(E)-162U (1974), Vol. 4, p. 42.
[47] F. Vivès, F.-J. Hambsch, H. Bax, and S. Oberstedt, Nucl. Phys. **A662**, 63 (2000).
[48] W. J. Maeck, W. A. Emel, A. L. Erikson, J. E. Delmore, and J. W. Meteer, *Symposium on Neutron Standards and Applications*, Gaithersburg, 1977, p. 146.
[49] L. Koch, NEANDC(E)-182 (1977), p. 5.
[50] W. J. Maeck, R. L. Eggleston, A. L. Erikson, and R. L. Tromp, *Symposium on Neutron Standards and Applications* (Ref. [48]) (1977), p. 186.
[51] W. Weinländer and H. J. Born, Radiochim. Acta **17**, 18 (1972).
[52] R. Michel and P. Nagel, *International Codes and Model Intercomparison for Intermediate Energy Activation Yields*, NEA report, NSC/DOC(97)-1, 1997.
[53] M. Blann, Annu. Rev. Nucl. Sci. **25**, 123 (1975).
[54] N. Bohr and J. Wheeler, Phys. Rev. **56**, 426 (1939).
[55] A. V. Ignatyuk, M. G. Itkis, V. N. Okolovich, G. N. Smirenkin, and A. S. Tishin, Yad. Fiz. **21**, 1185 (1975) [Sov. J. Nucl. Phys. **21**, 612 (1975)].
[56] S. Cohen, F. Plasil, and W. J. Swiatecki, Ann. Phys. (N.Y.) **82**, 557 (1974).
[57] A. S. Iljinov and M. V. Mebel, Nucl. Phys. **A543**, 517 (1992).
[58] V. P. Eismont, A. I. Obukhov, A. V. Prokofyev, and A. N. Smirnov, *Second International Conference on Accelerator Driven Transmutation Technologies and Applications*, Kalmar, Sweden, edited by H. Condé (Uppsala University, Stockholm, 1997), Vol. II, p. 592.
[59] M. G. Itkis, V. N. Okolovich, A. Ya. Rusanov, and G. N. Smirenkin, Yad. Fiz. **41**, 849 (1985) [Sov. J. Nucl. Phys. **41**, 544 (1985)].
[60] M. G. Itkis, N. A. Kondratev, Yu. V. Kotlov, S. I. Mulgin, V. N. Okolovich, A. Ya. Rusanov, and G. N. Smirenkin, Yad. Fiz. **47**, 7 (1988) [Sov. J. Nucl. Phys. **47**, 4 (1988)].
[61] M. C. Duijvestijn, A. J. Koning, J. P. M. Beijers, A. Ferrari, M. Gastal, J. van Klinken, and R. W. Ostendorf, Phys. Rev. C **59**, 776 (1999).
[62] C. M. Zöller, Ph.D. thesis, TH Darmstadt, 1995.
[63] J. F. Croall and J. G. Cuninghame, Nucl. Phys. **A125**, 402 (1969).
[64] D. G. Perry and F. W. Fairhall, Phys. Rev. C **4**, 977 (1971).
[65] J. Äystö, P. Dendooven, S. Hankonen, J. Jokinen, V. A. Rubchenya, W. H. Trzaska, D. N. Vakhtin, J. C. Wang, S. V. Khlebnikov, A. V. Kuznetsov, V. G. Lyapin, O. I. Osetrov, G. P. Tiourin, A. A. Alexsandrov, Yu. E. Penionzhkevich, Yu. V. Pyatkov, and Yu. G. Sobolev, *International Conference on Fission and Properties of Neutron-rich Nuclei*, edited by J. H. Hamilton, and A. V. Ramaya, Sanibal Island, Florida, 1997, p. 457.
[66] M. Thein, M. N. Rao, and P. K. Kuroda, J. Inorg. Nucl. Chem. **30**, 1145 (1968).
[67] D. R. Nethaway and B. Mendoza, Phys. Rev. C **2**, 2289 (1970).
[68] I. Winkelmann and D. C. Aumann, Phys. Rev. C **30**, 934 (1984).
[69] A. L. Prindle, D. H. Sisson, D. R. Nethaway, M. V. Kantelo, and R. A. Sigg, Phys. Rev. C **20**, 1824 (1979).
[70] C. Chung and J. J. Hogan, Phys. Rev. C **24**, 180 (1981).
[71] C. Chung and J. J. Hogan, Phys. Rev. C **25**, 899 (1982).
[72] P. Möller, Nucl. Phys. **A192**, 529 (1972).